Polycomb-mediated repression of EphrinA5 promotes growth and invasion of glioblastoma.

Barbara Ricci[1*], Thomas O. Millner[1*], Nicola Pomella[1], Xinyu Zhang[1], Loredana Guglielmi[1], Sara Badodi[1], Dario Ceric[1], Carolina Gemma[3], Erica Cognolato[1], Ying Zhang[2], Sebastian Brandner[2], Michael R. Barnes[4] and Silvia Marino[1+]

[1] Blizard Institute, Barts and The London School of Medicine and Dentistry, Queen Mary University of London, 4 Newark Street, London E1 2AT, UK

[2] Division of Neuropathology, the National Hospital for Neurology and Neurosurgery, University College London Hospitals NHS Foundation Trust, Queen Square, London WC1N 3BG, UK

[3] Department of Surgery and Cancer, Imperial College London, Hammersmith Hospital Campus, London W12 0NN, UK

[4] Centre for Translational Bioinformatics, William Harvey Research Institute, Barts and The London School of Medicine and Dentistry, Queen Mary University of London, London EC1M 6BQ, UK

* these authors contributed equally to this work

+ corresponding author

The authors declare no conflict of interest

Abstract

Glioblastoma (GBM) is the most common and most aggressive intrinsic brain tumour in adults. Integrated transcriptomic and epigenomic analyses of glioblastoma initiating cells (GIC) in a mouse model uncovered a novel epigenetic regulation of EfnA5. In this model, Bmi1 enhances H3K27me3 at the *EfnA5* locus and reinforces repression of selected target genes in a cellular context dependent fashion. EfnA5 mediates Bmi1-dependent proliferation and invasion *in vitro* and tumour formation in an allograft model. Importantly, we show that this novel Polycomb feed-forward loop is also active in human GIC and we provide preclinical evidence of druggability of the EFNA5 signalling pathway in GBM xenografts overexpressing Bmi1.

Introduction

Malignant gliomas are the most common intrinsic brain tumours in adults. They grow highly invasively, cannot be completely resected by surgery, and conventional anticancer treatments have limited efficacy, resulting in a dismal overall prognosis. Dysregulation of epigenetic mechanisms, together with genetic mutations, is an essential driver in the progression of malignant gliomas (reviewed in [1]). Therefore, to identify novel druggable targets, it is essential to elucidate the molecular mechanisms of this epigenetic dysregulation.

Polycomb group proteins (PcG) are chromatin associated proteins that maintain hereditable gene repression through histone modification and chromatin remodelling. At least two distinct PcG complexes have been identified, PRC1 and PRC2 (reviewed in [2]). PRC2 is composed of a catalytic subunit, Ezh2, which binds to Suz12 and EED to catalyse trimethylation of histone H3 at lysine 27 (H3K27me3), a *bona fide* epigenetic silencing mark. PRC1 depends upon PRC2 for recruitment to PcG target genes and is responsible for mono-ubiquitylation of histone H2A at lysine 119 (H2AK119u), an enzymatic activity dependent on the E3 ubiquitin ligase activity of Ring1B, which is enhanced by Bmi1. This sequence of events induces chromatin compaction and inhibition of transcription elongation (reviewed in [3]), although alternative mechanisms of action have also been described [4].
The role of several PcG genes, during the development of the mammalian central nervous system (CNS) and in the maintenance of postnatal stem cells in the adult brain, has been extensively characterised (reviewed in [5]). Loss of function studies in the mouse have shown that Bmi1 is essential for regulation of cell cycle entry of neural progenitors and for self-renewal of neural stem cells (NSC) [6-8]. These actions are, at least in part, mediated through transcriptional repression of the *ink4a* locus, encoding for $p16^{ink4a}$ and $p19^{arf}$ [6] and for the cell cycle inhibitor $p21^{waf1/cip1}$ [9, 10].

Cells with “stem-like” properties have been described in many cancers. These cells are essential for tumour maintenance and they frequently express stem cell genes as well as exhibit a stem cell-like chromatin structure. Bmi1 is highly expressed in glioblastoma stem/initiating cells (GIC) [11] and microRNAs - miR128 and miR218 - have been identified, which specifically block glioma self-renewal through Bmi1-downregulation [12, 13]. In keeping with these data, increased tumour latency and a shift toward glioma of a lower

histological grade were observed in an experimental murine glial tumour arising in ink4a/arf deficient mice bred into a *Bmi1-/-* background [14]. Interestingly, knockdown of BMI1 in human GIC (hGIC) significantly reduced tumour growth in a xenograft mouse model [15]. The role of Ezh2 in oncogenesis is also well characterised and it has been shown to be multimodal. In gliomagenesis, somatic mutations of histone H3 variant H3F3A have been described in paediatric tumours (DIPGs), leading to depletion of H3K27me3 on canonical H3 because of inhibition of PRC2 activity [16]. EZH2 has also been shown to contribute to the pathogenesis of adult high grade gliomas (HGG) via a non-histone mediated interaction with STAT3. In this case, the trimethylation of STAT3 at K180 by EZH2 was essential for aberrant STAT3 activation in GIC [17], a finding known to be associated with poor survival in patients with GBM [18]. There is likely a complex interplay between BMI1 and EZH2 in GBM and recent evidence shows that strategies that simultaneously target multiple epigenetic regulators may be required to control GBM growth [19].

We have recently demonstrated that conditional overexpression of Bmi1 has a different functional impact on CNS development depending on the differentiation stage of neural precursor cells [20], and that this is mediated by the amount of H3K27me3 at the promoter region of selected target genes in a cell-context dependent fashion [21]. We have also shown that GIC isolated from a mouse model of HGG [22] show a similar epigenetic regulation of Bmi1 target genes [21]. These data are in keeping with increased H3K27me3 being a general mechanism mediating the functional outcome of elevated Bmi1 expression in both non-neoplastic and neoplastic contexts.

Here we have used a combined genome-wide and target gene-driven approach to comprehensively identify target genes and pathways mediating Bmi1 function specifically in GIC as compared to NSC. The availability of non-neoplastic NSC engineered to overexpress Bmi1 allowed us to mimic the physiological fluctuation of Bmi1 expression during neural differentiation.

Material and Methods

Generation of mice and genotyping

Transgenic *STOPFloxBmi1* mice were previously generated in our laboratory [21]. Activation of Bmi1 overexpression was obtained in embryos by crossing *STOPFloxBmi1* and *NestinCre* mice to generate double transgenic animals, as previously described [21].

Cultures

Primary NSC cultures were prepared from E16.5 *STOPFloxBmi1;NestinCre* transgenic and control wild type embryos. Primary mouse $PTEN^{F/F};P53^{F/F}$ NSC and mGIC were cultured as adherent cells in Neurobasal and DMEM/F12 media containing N2 and B27 supplements and human recombinant FGF and EGF.

ChIPSeq and RNASeq

RNASeq: After trimming and quality control, reads were aligned to the mm10 mouse genome using STAR. Trimmed mean of M-values (TMM) normalization was applied to the dataset and differential expression (DE) analysis was performed using the Bioconductor package edgeR in R [23], with a Quasi-Likelihood F-test (QLF) and an FDR cut-off of 0.05.

ChIPSeq: After trimming and quality control, reads were aligned to the mm10 mouse genome using Bowtie v2.3.4 (sourceforge.net/projects/bowtie-bio/files/bowtie2/), allowing up to one mismatch per read and discarding multi-mapped reads. The MACS2 algorithm [24] was used to call H3K27me3 peaks (subroutine *callpeak*) and perform the differential binding (DB) analysis (subroutine *bdgdiff*).

Proximity Ligation Assay

We cloned a 578 bp region spanning chr17:62687621-62688198 for EfnA5 locus into a TOPO TA Cloning vector. 1µg of plasmid DNA was used as template to generate a biotintylated probe. Slides with attached cells were then incubated with probes, followed by ligation and amplification steps. Anti-mCherry antibody was used to detect transfected cells.

***In Vitro* Functional Assays**

Proliferation, wound healing scratch assay and invasion assay for mGIC were imaged with IncuCyte ZOOM/Live-Cell Software (EssenBioScience) or INCell 2200 (GE Healthcare) with Developer Toolbox software (GE Healthcare).

Orthotopic transplantation of GIC into NODSCID mice and bioluminescence imaging (BLI)

6-12 week old NODSCID mice were anaesthetised and $5x10^5$ mGIC were injected into the right cerebral hemisphere with the following coordinates from the bregma suture: 2 mm posterior, 2 mm lateral, 4 mm deep, 10° angle. Tumour formation and growth was assessed by BLI for mGIC xenografts.

***In vivo* treatment with doxazosin**

100mg/kg of doxazosin was given daily by subcutaneous injection and 100mg/kg elacridar was given by oral gavage every second or third day, 4 hours prior to doxazosin dose. Experimental animals (n=8 for each group) were treated with elacridar and vehicle control, or elacridar and doxazosin. Mice were culled after treatment and brains removed for histological assessment.

All further methods and additional details are included as supplementary material.

Results

Differential redistribution of the H3K27me3 mark in mGIC as compared to NSC.

In order to define the cellular pathways deregulated in gliomagenesis in a Bmi1-dependent, H3K27me3-mediated manner, we used a well-established mouse model of gliomagenesis that relies on the loss of *PTEN* and *p53*, two of the most common genetic alterations in *IDH* wild type glioblastoma (GBM) [25]. The model relies on Adeno-Cre-mediated recombination of floxed alleles, either by intraventricular virus injection or by *in vitro* treatment of NSC prior to their intracerebral injection [22]. HGG develop with good penetrance in this model and cells with tumour initiating properties (mGIC) can be effectively propagated in culture. Our previous findings have shown overexpression of Bmi1 and increased global levels of H3K27me3 in these cells, as compared to NSC [21].

We performed ChIPSeq for H3K27me3 and RNASeq to investigate the genome-wide correlation between the redistribution of this PRC2 mark and its transcriptional impact in gliomagenesis. To mimic the physiological fluctuation of Bmi1 expression in NSC we compared mGIC to non-neoplastic NSC expressing basal or increased ($Bmi1^{Over}$) levels of Bmi1 (Fig.1A). Two biologically independent NSC cultures, two NSC $Bmi1^{Over}$ cultures, isolated from *NestinCre;STOPFloxBmi1* and two mGIC cultures were used for this study.

Analysis of the ChIPSeq datasets using MACS2 identified unique peaks in the neoplastic (cluster A) and non-neoplastic (cluster B) Bmi1 overexpressing context (Fig.1B-C). Pathway analysis on the Ingenuity Pathway Analysis (IPA) platform identified Axonal Guidance Signalling, Glioblastoma Multiforme Signalling, Role of Wnt/GSK-3β signalling and Ephrin A Signalling, among others, as enriched in mGIC (Fig.S1A).

Comparisons of the transcriptome of mGIC vs NSC, and mGIC vs NSC Bmi1^{Over} identified 7319 shared differentially expressed genes (Fig.1D; 91% and 84% of all deregulated genes, respectively), of which 3813 were specifically down-regulated in mGIC (Fig.1E). We chose to validate 13 genes that were enriched in pathways of interest, or highlighted as likely to be important in GBM pathobiology after thorough literature review. Of these genes, 10/13 were confirmed to be reduced specifically in mGIC in biological replicas of NSC, NSC Bmi1^{Over} and mGIC (Fig.1G).

To determine the molecular pathways that are transcriptionally regulated by the PRC2-mediated H3K27me3 mark, we integrated the RNASeq and ChIPSeq datasets. This identified a core subset of 231 genes that had acquired the H3K27me3 mark in mGIC but not NSC or NSC Bmi1^{Over} (defined as “unique”), and that also had concomitant reduced expression (defined as “concordant”) (Fig.1F). These 231 genes showed significant overlap with 33 datasets of the NIH Roadmap Epigenomics H3K27me3 ChIPSeq database (http://www.roadmapepigenomics.org/) (Fig.S1B).

To begin to assess the translational value of our findings in human GBM, this core subset of genes was comparatively analysed in a publicly available H3K27me3 ChIPSeq dataset of human GIC [26]. 97/231 genes shared the mark in both mGIC and hGIC (Fig.S1C), and a high overlap was found in the molecular pathways that were enriched in both mouse and human contexts (Fig.1H).

Transcriptional regulation is Bmi1-dependent in a proportion of H3K27me3 marked genes.

To assess which of the genes identified in the screening described above were dependent on Bmi1 expression, we silenced Bmi1 in mGIC cultures with shRNA (Fig.2A) and then assessed the expression levels of the genes previously validated. We found that 2/10 validated genes, EfnA5 and Jph3, were upregulated upon Bmi1 silencing, demonstrating that

their regulation is Bmi1-dependent (Fig.2B). Up-regulation of EfnA5 upon Bmi1 silencing was confirmed at the protein level by means of western blot (Fig.S2A).

Our ChIPSeq data showed widespread enrichment for H3K27 trimethylation at the *EfnA5* locus in mGIC, as compared to both NSC and NSC Bmi1^{Over}, which was accompanied by reduced expression with RNASeq (Fig.2C). A similar pattern of H3K27me3 enrichment at the *EFNA5* locus (Fig.S2B) and reduced expression (Fig.S2C) was observed when we analysed published data from hGIC [26].

ChIP for H3K27me3, followed by qPCR for *EfnA5* in mGIC upon silencing of Bmi1, confirmed that H3K27me3 enrichment was dependent on the expression levels of Bmi1 (Fig.2D).

These data are in keeping with a Bmi1-mediated regulation of *EfnA5* via modulation of the levels of H3K27me3 at its promoter in our GBM mouse model.

Bmi1 controls H3K27me3 levels at the *EfnA5* locus via downregulation of JmjD3 in mGIC.

In order to maintain a cell-type-specific expression pattern, H3K27me3 at specific gene loci is finely regulated by histone methylase and demethylase activity [27, 28]. We have previously demonstrated that NSC overexpressing Bmi1 show reduced expression of the demethylase JmjD3, but no significant changes in expression levels of the methylase Ezh2, suggesting that Bmi1 might control the H3K27me3 repressive mark through the downregulation of JmjD3 [21]. To test the potential contribution of JmjD3 in the regulation of H3K27me3 levels in our model, we performed a proximity ligation assay (PLA) for H3K27me3 on the *EfnA5* locus (Fig.S3 and Fig.3A) upon overexpression of JmjD3 vs treatment with an Ezh2 inhibitor (Ezh2i).

We show that increased expression of JmjD3 in mGIC (shScr+JmjD3; Fig.3B top right panel and Fig.3C) led to a significantly reduced H3K27me3 at the *EfnA5* locus as compared to shScr (Fig.3B top left panel and Fig.3C) and shScr treated with Ezh2i (shScr+Ezh2i; Fig.3B top middle panel and Fig.3C), confirming that JmjD3 plays a major role in regulating the levels of H3K27me3 at the *EfnA5* locus in mGIC. In keeping with this interpretation, cells overexpressing JmjD3 and further treated with Ezh2i (shScr+JmjD3+Ezh2i; Fig.3B bottom left panel) did not show any significant additional decrease of the H3K27me3 signal as compared to shScr+JmjD3 only (Fig.3C). Similar results were observed in both shBmi1 and

shBmi1+Ezh2i cells (Fig.3B bottom middle and bottom right panels, respectively), showing a decreased level of H3K27me3 upon Bmi1 silencing compared to shScr, but no significant additional change when Ezh2i was added. Off-target effects were also ruled out (Fig.3D).

We conclude that Bmi1 regulates the levels of H3K27me3 via repression of JmjD3 in mGIC (see Fig.S3B for schematic).

Bmi1 regulates cell morphology, proliferation and migration/invasion via repression of EfnA5 in mGIC.

We have shown above that EfnA5 is upregulated upon Bmi1 silencing. Therefore, we next set out to assess *in vitro* the functional role of EfnA5 as a mediator of the Bmi1-dependent phenotype of mGIC. We used pre-clustered recombinant mouse EfnA5 Chimera-Fc (rmEfnA5-Fc) to activate EfnA5 forward signalling [29].

EfnA5 regulates focal adhesion, cell motility and cancer invasion via modulation of the actin cytoskeleton [30, 31], therefore we assessed whether upregulation of EfnA5 upon shBmi1 affected cellular architecture in our model. We evaluated the formation of stress fibres, with phalloidin staining, as a measure of EfnA5-mediated activation of focal adhesion as well as cellular process length with GFAP staining. When we compared rmEfnA5-Fc treated mGIC with shBmi1 mGIC, phalloidin intensity was similar (Fig.4A), and cellular process length was increased in both conditions. These data support the interpretation that exogenous EfnA5 modifies the cytoskeleton and cell morphology in a similar fashion to Bmi1 knockdown, which leads to an endogenous overexpression of EfnA5.

Next, we assessed whether EfnA5 repression contributed to the previously described [15] Bmi1-mediated regulation of cellular proliferation. mGIC treated with rmEfnA5-Fc showed significantly decreased proliferation, with a similar decrease observed in shBmi1 mGIC (Fig.4C). Expression of $p16^{ink4a}$, $p19^{arf}$ and p21 was not significantly upregulated in this model (Fig.S2D).

Additionally, shBmi1 mGIC showed reduced migration potential (Fig.4D), in keeping with previous reports [14]. A similar phenotype was also observed when mGIC were treated with rmEfnA5-Fc, raising the possibility that modulation of EfnA5 expression levels may contribute to Bmi1-mediated regulation of cell migration.

To assess whether the upregulation of EfnA5 expression observed upon Bmi1 silencing was responsible for the observed phenotype, we used shRNA to knockdown EfnA5 in shBmi1 mGIC (Fig.S4A; 'shEfnA5', with 'shmCherry' as the reporter-matched scrambled control). Interestingly, silencing of EfnA5 in shBmi1 mGIC, neutralised the effect of Bmi1 knockdown on stress fibre formation and cellular process length (Fig.5A). Importantly, the decreased proliferation rate observed in shBmi1 mGIC, as assessed by live imaging (Fig.5B and Fig.S4B) and neurosphere assay (Fig.S4D and Fig.S5A), was also rescued when concomitant silencing of EfnA5 was carried out, a finding supported by the lack of significant impact of Bmi1 silencing on the expression of cell cycle inhibitors in our model (Fig.S2D). Silencing of EfnA5 in shBmi1 mGIC also rescued the migration defect observed in shBmi1 mGIC (Fig.5C and Fig.S4C). Finally, shBmi1 mGIC showed reduced invasion through a 3D collagen gel, which was also rescued by concommitant shEfnA5 (Fig.S5B).

Taken together our data show that repression of EfnA5 plays a key role in mediating Bmi1 function in the regulation of key mGIC properties *in vitro*.

Repression of EfnA5 by Bmi1 is essential for glioblastoma development in an allograft model.

Given these important roles in proliferation, migration and invasion, we asked whether EfnA5 might also mediate the impact of Bmi1 on tumourigenesis *in vivo*. Analytical imaging of NODSCID mice with orthotopically implanted luciferase-tagged mGIC revealed that while 5/9 mice injected with control mGIC developed tumours and silencing of Bmi1 strongly suppressed tumour growth (0/9), concomitant silencing of EfnA5 and Bmi1 rescued tumour incidence (6/9) (Fig.6A,B). Histological analysis of the engrafted brains revealed high grade glial tumours composed of cells with enlarged, pleomorphic and occasionally hyperchromatic nuclei, frequent mitoses and areas of necrosis (Fig.6C and S6A,B). Immunostaining for GFAP, Olig2 and Sox2 confirmed the glial nature of these neoplasms (Fig.6C).

These data show that repression of EfnA5 plays a key role in mediating the tumourigenic role of Bmi1 *in vivo*.

BMI1 also regulates cell proliferation via repression of EFNA5 in hGIC.

To understand whether our findings could be translatable to human GBM, we assessed whether a significant correlation existed between BMI1 and EFNA5 expression in human tumours. We used published RNA microarray, RNASeq and single-cell RNASeq datasets from The Cancer Genome Atlas (TCGA), the National Center for Biotechnology Information (NCBI) Gene Expression Omnibus (GEO) databanks and gbmseq.org [32]. Of the TCGA datasets, we found that the dataset with the highest number of tumour samples (hthgu133a, n=548) showed a strong and significant inverse correlation between BMI1 and EFNA5 (Fig.S7A), whilst the other three datasets did not (data not shown). Next, we interrogated two independent GBM single-cell RNAseq datasets [32, 33], and confirmed that a significant number of tumour cells displayed a negative association between BMI1 and EFNA5 (Fig.7A and Fig.S7B). Furthermore, we sought to establish whether this negative correlation was found in hGIC specifically by analysing two datasets of primary patient-derived cultured hGIC characterised with RNA microarray (GSE89399 [34]) and RNASeq (GSE89623 [35]). Both of these independent hGIC cohorts displayed a strong and significant negative correlation between BMI1 and EFNA5 (Fig.7B,C).

Next, we tested whether the functional role for the Bmi1/EfnA5 axis observed in mGIC was also present in hGIC *in vitro*. To this end, the Human Glioblastoma Cell Culture resource (HGCC.se [36]) was interrogated. An inverse correlation between the expression of BMI1 and EFNA5 was again observed, although it did not reach statistical significance (data not shown). Interestingly, these 48 hGIC lines could be clustered into two subgroups on the basis of the expression levels of BMI1 and EFNA5, with a strong and significant negative correlation of BMI1 and EFNA5 being observed in primary lines belonging to the Proneural molecular subtype (n=9; Fig.7D).

We selected two of these primary Proneural hGIC lines (U3118 and U3033) to examine the translational potential of the BMI1/EFNA5 pathway. Upon BMI1 knockdown with shRNA, we observed a corresponding increase in EFNA5 levels (Fig.7E), and a significant decrease in proliferation in both lines (Fig.7H and Fig.S7D). Ephrin downstream signal transduction is activated by a complex process that requires the assembly of higher-order ligand and receptor clusters for signalling initiation [29]. Therefore, pre-clustering of recombinant EfnA5 protein (as we have used with mGIC above) results in activation of the signalling

pathway. However, if recombinant protein is added without prior clustering it blocks the Ephrin receptor sites and inhibits Ephrin pathway signaling [37]. In both lines, activation of the EFNA5 signalling pathway was observed upon BMI1 knockdown, which was rescued by pathway blockade with recombinant proteins, as confirmed by immunofluorescence staining for phosphorylation of selected Eph receptors (U3118 shown in Fig.7F). We used recombinant chimera-Fc protein for human EFNA5 as well as two of its receptors, EPHA4 and EPHA5, for this pathway inhibition. We show that the decreased proliferation rate observed in hGIC after BMI1 knockdown was rescued with concomitant inhibition of the EFNA5 signalling pathway in U3118 and U3033 (Fig.7H and Fig.S7D, respectively). These data were supported by EdU staining that showed the same decrease upon BMI1 knockdown and rescue with EFNA5 pathway inhibition (Fig.7G and Fig.S7C).

These data are in keeping with the interpretation that repression of EFNA5 also plays an important role in mediating BMI1 function in hGIC.

Doxazosin effectively targets BMI1^{high}/EFNA5^{low} hGIC *in vitro* and *in vivo*.

Next, we set out to test the hypothesis that pharmacologically targeting the EFNA5 pathway is effective against hGIC expressing high BMI1 levels. In cells with high levels of BMI1, EFNA5 is repressed, therefore we identified a drug that mimicked EFNA5 action. Doxazosin is a small molecule agonist for Eph receptors for which EFNA5 acts as a ligand (EphA2 and EphA4) [38], independent of the α1-adrenoceptor action for which it is commonly used clinically. Upon treatment of U3118shScr and U3118shBMI1 cells with 5μM doxazosin, proliferation was significantly more impacted in the U3118shScr than it was in the shBMI1 condition (Fig.8A). Indeed, there was a significant large decrease in proliferation with doxazosin treatment in the shScr group, whilst there was only a small, non-significant difference in the shBMI1 group after eight days (Fig.8B). Assessment of EphA2-4 phosphorylation (targets of EFNA5) in shScr and shBMI1 cells upon exposure to doxazosin confirmed activation of the pathway (Fig.8C,D). Decreased levels of phosphorylation of ERK1/2, a known downstream effectors of EphA2 [38], were also detected in shScr cells that were treated with doxazosin, whilst in shBMI1 cells this was not the case (Fig.8C,D).

We next wanted to see if the results we had observed with doxazosin *in vitro* could be translated to an *in vivo* setting. Firstly, we established that doxazosin could cross the blood-brain barrier (BBB) in mice by assessing the levels of the drug in the serum and brain homogenate by liquid chromatography – mass spectrometry (LC-MS) after subcutaneous injections of doxazosin (50mg/kg). The levels of doxazosin in the serum of NODSCID mice reached a peak of nearly 4000ng/mL, 1 hour after injection, whilst the levels in brain homogenate reached a peak of ~50ng/mg after 2 hours (Fig.S8A), a timeframe comparable to that seen in rats [39]. Only approximately 1% of the doxazosin in the serum was entering the brain after subcutaneous injection of doxazosin. The BBB efflux transporter inhibitor elacridar has been shown to be effective pre-clinically in enhancing brain accumulation upon dual administration with several anti-glioma agents [40]. Although it is not known if doxazosin is excreted by these transporters, prazosin, another commonly used α1-adrenoreceptor antagonist sharing high structural similarity with doxazosin, is known to be excreted by these transporters [41, 42]. Two doses of doxazosin, 50 and 100 mg/kg, were combined with either a vehicle control or 100mg/kg of elacridar (given by oral gavage four hours before doxazosin dose), and the levels of doxazosin were again measured in the serum and brain homogenate of mice. The levels of doxazosin in the serum were not significantly different across the groups, whilst the levels of doxazosin were significantly greater in brain homogenate when doxazosin was combined with elacridar (Fig.S8B), reaching levels nearly 10 times higher than doxazosin alone, at the higher doxazosin dose. We also found that, in agreement with other studies [38, 43], doxazosin did not have any significant side effects in experimental animals.

We intracranially injected 0.5 x 10^6 U3118shScr and U3118shBMI1 cells into NODSCID mice. U3118 xenografts have a median survival of ~37 weeks [34]. To assess the effect of doxazosin at an early tumour stage, at 16 weeks eight mice of each shScr and shBMI1 were assigned to either 100mg/kg elacridar and vehicle, or 100mg/kg elacridar + 100mg/kg doxazosin. Mice were culled after treatment and tumour volume (immunohistochemistry for human vimentin) and proliferation (Ki67 staining) and apoptosis (cleaved caspase3 staining) were assessed. Tumour volume was significantly reduced after doxazosin treatment in the shScr cells, whereas there was no significant reduction in shBMI1 xenografts (Fig.8E,F). Proliferation was reduced upon drug treatment in shScr group but not

in the shBMI1 group (Fig.8E,G). No evidence of cCASP3 positive cells was found. All tumours showed cells with enlarged, pleomorphic and occasional hyperchromatic nuclei on H&E, whilst all conditions show diffuse staining for GFAP (cytoplasmic) and SOX2 (nuclear), with a smaller fraction positive for OLIG2 (Fig.S8C).

This data provides preclinical evidence in GBM xenografts that the EFNA5 agonist, doxazosin, is effective against early stages of GBM derived from GIC with a $BMI1^{high}/EFNA5^{low}$ molecular signature.

Discussion

We show here a novel epigenetic regulation of EfnA5 in a mouse model of GBM. This highlights a novel Polycomb feed-forward loop in gliomagenesis, whereby PRC1 reinforces repression of selected target genes in a cellular context-dependent fashion.

Consistent with the critical roles of P53 and PTEN-PI3K-AKT alterations in GBM pathogenesis, GBM genomic and proteomic profiles from TCGA show significant correlation between higher levels of AKT activation and poorer prognosis in patients with *P53* mutations [44]. To model these pathway alterations, mGIC isolated from HGG arising from NSC/NPC upon intraventricular Adeno-Cre mediated recombination of $p53^{F/F}/PTEN^{F/F}$ [22] were used. We demonstrate that repression of EfnA5 expression via increased trimethylation of H3K27 is a core mechanism mediating the functional outcome of the high levels of Bmi1 seen in $p53^{-/-};PTEN^{-/-}$ mGIC. We did not observe an impact on ink4a/arf in this model, in keeping with existing literature showing a non-functional ink4a/arf pathway in a *p53* knockout setting [16, 45].

The Ephrin / Eph receptor family comprises 8 ligands (Efn: Eph Receptor Interacting ligand) and 14 type I transmembrane receptor tyrosine kinases (Eph: Erythropoietin-Producing Human Hepatocellular receptors), which are classified into type A and B, whereby 9 EphA and 5 EphB receptors promiscuously bind 5 EfnA ligands and 3 EfnB ligands, respectively (reviewed in [46]). Ephrins and Eph receptors are variably expressed in different cells at varying stages of differentiation and play essential roles in the control of cell morphology, adhesion, movement, proliferation and differentiation in embryonic development and tissue

homeostasis. In addition, they are often up-regulated in injured tissues, where they inhibit regenerative processes and promote angiogenesis. They are known to be frequently deregulated in cancer, including glioblastoma, being either overexpressed or down-regulated (reviewed in [47]). Moreover EphA2 and EphA3, receptors for the ligand EFNA5, are markers of poorer outcome in GBM and are involved in proliferation, invasion and neovascularisation [48]. The regulatory mechanisms governing the expression of Ephrins and Eph receptors have been extensively studied. The transcription factors HOXA1 and HOXB1 have been shown to activate EphA2 expression in the developing mouse brain [49]. Hypermethylation at CpG islands of promoter regions of many Ephrins, including EfnA5, and Eph receptors have been demonstrated in acute lymphoblastic leukaemia [50] and miRNAs, such as miR-210 and miR-26b, have been shown to down-regulate the expression of EfnA1 in hepatic ischaemia [51] and EphA2 in gliomas [52]. Importantly, Bmi1 is known to regulate miRNAs, such as miR10a [53] that has been shown to repress EphA8 in glioma cells, mediating the epithelial-mesenchymal transition and promoting cell migration and invasion [54]. *EfnA5* is reported as a miR-10a-3p target in the miRBase database (http://www.mirbase.org/).

Using a genome-wide approach, we show that a novel regulation of *EfnA5* via PcG-mediated histone tail modification is specific to the neoplastic context, and that normal NSC and NSC overexpressing Bmi1 did not reveal similar regulation (Fig.S3B). We also found that the repression of EfnA5 by Bmi1 contributes to tumour growth *in vitro* and *in vivo* in our mouse model.

The aberrant retention of H3K27me3 as a common epigenetic mechanism mediating the phenotype of Bmi1 overexpression opens a novel conceptual entry point into the interrogation of the role of Bmi1 in gliomagenesis. We show that repression of JmjD3 significantly contributes to the increased H3K27me3 at selected target genes in a mouse model. JmjD3 is the first demethylase to have been shown to antagonise Polycomb silencing, and is required for early neural commitment [55, 56]. ChIPSeq experiments have shown that it is a direct Bmi1/PRC1 target in various model systems [57, 58]. JmjD3 also plays a critical role in late neurogenesis [59]. JmjD3 is induced during differentiation of hGIC, where it promotes a differentiation-like phenotype via chromatin dependent (*ink4a/arf* locus activation) and chromatin independent (nuclear p53 protein stabilisation) mechanisms

[60]. Moreover, ChIPSeq analysis in embryonic stem cells (ESC) expressing a GFP-tagged version of JmjD3, revealed that JmjD3 targets are enriched in molecular pathways that are critically involved in gliomagenesis. These include the direct regulation of *Mdm2* and *Akt2* as well as the regulation of genes such as *Stat3* and *Rhpn2*, which are involved in GBM Mesenchymal transformation and as downstream effectors of GBM genomic lesions, respectively [61, 62]. Finally, pharmacological inhibition of JmjD3 has been shown to impair the tumourigenic potential of H3K27M DIPG cells by restoring normal levels of H3K27me3 [63].

Our data delineate a novel PcG feed forward loop in which Bmi1 enhances its repressive efficacy at specific target genes in mGIC by increasing H3K27me3-mediated gene repression. We show that the modulation of EfnA5 expression via regulation of H3K27me3 levels is mGIC specific, thus raising the possibility that a multi-layered regulatory mechanism is at play at a locus playing a key role in gliomagenesis.

We also report that an inverse correlation of gene expression of BMI1/EFNA5 is found in human GBM and in hGIC, and we provide initial evidence that repression of EFNA5 mediates, at least in part, the role of BMI1 in regulating hGIC proliferation. Existing literature in human cells has shown that EFNA5 acts as a tumour suppressor gene in GBM via negative regulation of EGFR [64], thus providing an interpretative framework for the requirement of an epigenetic regulation of this protein in GBM.

The wealth of suggestive evidence linking perturbations in H3K27 methylation to the development of malignant gliomas indicates that it will be essential to further explore whether and how this epigenetic mark could be a rational target for epigenetic therapy to counteract tumour maintenance in GBM. Moreover, Eph receptor / Ephrin signalling pathways are a promising area for anti-cancer therapies with strategies for their therapeutic targeting already developed with some already in clinical trials [65]. Here we show that doxazosin, an EFNA5 mimic, inhibits proliferation of GIC in a BMI1-dependent fashion. We demonstrate that doxazosin inhibits the ERK pathway, as assessed by its decreased phosphorylation. We also show that doxazosin is able to cross the BBB in combination with an efflux transporter inhibitor. When GIC were orthotopically xenografted into NODSCID mice, treatment with doxazosin recapitulated the *in vitro* findings in early stage tumours: tumour size was significantly decreased in the shScr tumours with concomitant decreased

proliferation, whilst there was no difference in shBMI1 tumours. Together these results provide pre-clinical evidence that precision targeting of Eph receptor / ephrin signalling [66] could be an effective therapeutic tool in GBM overexpressing BMI1.

Acknowledgements

This work is funded by grants from the MRC (1365533.studentship to BR), The Brain Tumour Charity (GN-000389 clinical research training fellowship to TM and BTC 8/128 to SB), Barts Charity (project and programme grants to SM) and Brain Tumour Research (Centre of Excellence award to SM); YZ was supported by a PhD Overseas research scholarship, UCL – ORS and UCLH Trustees. This research also forms part of the research themes contributing to the translational research portfolio of Barts and the London Biomedical Research Centre, which is supported and funded by the National Institute of Health Research. LC-MS measurements of doxazosin were carried out by Dr Roberto Buccafusca, SBCS Mass Spectrometry Facility, QMUL. All xenograft tumour histology was performed by IQPath, UCLH, London.

References

1 Timp W, Feinberg AP. Cancer as a dysregulated epigenome allowing cellular growth advantage at the expense of the host. *Nature reviews* (Research Support, N.I.H., Extramural) 2013; 13: 497-510.

2 Entrevan M, Schuettengruber B, Cavalli G. Regulation of Genome Architecture and Function by Polycomb Proteins. *Trends Cell Biol* 2016; 26: 511-525.

3 Blackledge NP, Rose NR, Klose RJ. Targeting Polycomb systems to regulate gene expression: modifications to a complex story. *Nat Rev Mol Cell Biol* 2015; 16: 643-649.

4 Gil J, O'Loghlen A. PRC1 complex diversity: where is it taking us? *Trends Cell Biol* (Research Support, Non-U.S. Gov't) 2014; 24: 632-641.

5 Testa G. The time of timing: How Polycomb proteins regulate neurogenesis. *Bioessays* 2011.

6 Jacobs JJ, Kieboom K, Marino S, DePinho RA, van Lohuizen M. The oncogene and Polycomb-group gene bmi-1 regulates cell proliferation and senescence through the ink4a locus. *Nature* 1999; 397: 164-168.

7 Lessard J, Sauvageau G. Bmi-1 determines the proliferative capacity of normal and leukaemic stem cells. *Nature* 2003.

8 Voncken JW, Schweizer D, Aagaard L, Sattler L, Jantsch MF, van LM. Chromatin-association of the Polycomb group protein BMI1 is cell cycle-regulated and correlates with its phosphorylation status. *Journal of cell science* 1999; 112 (Pt 24): 4627-4639.

9 Fasano CA, Dimos JT, Ivanova NB, Lowry N, Lemischka IR, Temple S. shRNA knockdown of Bmi-1 reveals a critical role for p21-Rb pathway in NSC self-renewal during development. *Cell stem cell* 2007; 1: 87-99.

10 Subkhankulova T, Zhang X, Leung C, Marino S. Bmi1 directly represses p21Waf1/Cip1 in Shh-induced proliferation of cerebellar granule cell progenitors. *Molecular and cellular neurosciences* 2010; 45: 151-162.

11 Hemmati HD, Nakano I, Lazareff JA, Masterman-Smith M, Geschwind DH, Bronner-Fraser M *et al*. Cancerous stem cells can arise from pediatric brain tumors. *Proceedings of the National Academy of Sciences of the United States of America* 2003; 100: 15178-15183.

12 Godlewski J, Nowicki MO, Bronisz A, Williams S, Otsuki A, Nuovo G *et al*. Targeting of the Bmi-1 oncogene/stem cell renewal factor by microRNA-128 inhibits glioma proliferation and self-renewal. *Cancer research* 2008; 68: 9125-9130.

13 Tu Y, Gao X, Li G, Fu H, Cui D, Liu H *et al*. MicroRNA-218 inhibits glioma invasion, migration, proliferation, and cancer stem-like cell self-renewal by targeting the polycomb group gene Bmi1. *Cancer research* 2013; 73: 6046-6055.

14 Bruggeman SW, Hulsman D, Tanger E, Buckle T, Blom M, Zevenhoven J *et al*. Bmi1 controls tumor development in an Ink4a/Arf-independent manner in a mouse model for glioma. *Cancer cell* 2007; 12: 328-341.

15 Abdouh M, Facchino S, Chatoo W, Balasingam V, Ferreira J, Bernier G. BMI1 sustains human glioblastoma multiforme stem cell renewal. *J Neurosci* 2009; 29: 8884-8896.

16 Mohammad F, Weissmann S, Leblanc B, Pandey DP, Hojfeldt JW, Comet I *et al*. EZH2 is a potential therapeutic target for H3K27M-mutant pediatric gliomas. *Nature medicine* 2017; 23: 483-492.

17 Kim E, Kim M, Woo DH, Shin Y, Shin J, Chang N *et al*. Phosphorylation of EZH2 activates STAT3 signaling via STAT3 methylation and promotes tumorigenicity of glioblastoma stem-like cells. *Cancer cell* (Research Support, N.I.H., Extramural

Research Support, Non-U.S. Gov't) 2013; 23: 839-852.

18 Carro MS, Lim WK, Alvarez MJ, Bollo RJ, Zhao X, Snyder EY *et al*. The transcriptional network for mesenchymal transformation of brain tumours. *Nature* (Research Support, N.I.H., Extramural

Research Support, Non-U.S. Gov't) 2010; 463: 318-325.

19 Jin X, Kim LJY, Wu Q, Wallace LC, Prager BC, Sanvoranart T *et al*. Targeting glioma stem cells through combined BMI1 and EZH2 inhibition. *Nature medicine* 2017; 23: 1352-1361.

20 Yadirgi G, Leinster V, Acquati S, Bhagat H, Shakhova O, Marino S. Conditional activation of Bmi1 expression regulates self-renewal, apoptosis, and differentiation of neural stem/progenitor cells in vitro and in vivo. *Stem cells (Dayton, Ohio)* 2011; 29: 700-712.

21 Acquati S, Greco A, Licastro D, Bhagat H, Ceric D, Rossini Z *et al*. Epigenetic regulation of survivin by bmi1 is cell type specific during corticogenesis and in gliomas. *Stem cells (Dayton, Ohio)* 2013; 31: 190-202.

22 Jacques TS, Swales A, Brzozowski MJ, Henriquez NV, Linehan JM, Mirzadeh Z *et al*. Combinations of genetic mutations in the adult neural stem cell compartment determine brain tumour phenotypes. *The EMBO journal* 2010; 29: 222-235.

23 Robinson MD, McCarthy DJ, Smyth GK. edgeR: a Bioconductor package for differential expression analysis of digital gene expression data. *Bioinformatics (Oxford, England)* 2010; 26: 139-140.

24 Zhang Y, Liu T, Meyer CA, Eeckhoute J, Johnson DS, Bernstein BE *et al*. Model-based analysis of ChIP-Seq (MACS). *Genome Biol* 2008; 9: R137.

25 Sturm D, Witt H, Hovestadt V, Khuong-Quang DA, Jones DT, Konermann C *et al*. Hotspot mutations in H3F3A and IDH1 define distinct epigenetic and biological subgroups of glioblastoma. *Cancer cell* 2012; 22: 425-437.

26 Rheinbay E, Suva ML, Gillespie SM, Wakimoto H, Patel AP, Shahid M *et al*. An aberrant transcription factor network essential for Wnt signaling and stem cell maintenance in glioblastoma. *Cell Rep* 2013; 3: 1567-1579.

27 Agger K, Cloos PA, Christensen J, Pasini D, Rose S, Rappsilber J *et al*. UTX and JMJD3 are histone H3K27 demethylases involved in HOX gene regulation and development. *Nature* 2007; 449: 731-734.

28 Sparmann A, van Lohuizen M. Polycomb silencers control cell fate, development and cancer. *Nature reviews* 2006; 6: 846-856.

29 Himanen JP, Yermekbayeva L, Janes PW, Walker JR, Xu K, Atapattu L *et al*. Architecture of Eph receptor clusters. *Proceedings of the National Academy of Sciences of the United States of America* 2010; 107: 10860-10865.

30 Wozniak MA, Modzelewska K, Kwong L, Keely PJ. Focal adhesion regulation of cell behavior. *Biochimica et biophysica acta* 2004; 1692: 103-119.

31 Zhong C, Kinch MS, Burridge K. Rho-stimulated contractility contributes to the fibroblastic phenotype of Ras-transformed epithelial cells. *Mol Biol Cell* 1997; 8: 2329-2344.

32 Darmanis S, Sloan SA, Croote D, Mignardi M, Chernikova S, Samghababi P *et al*. Single-Cell RNA-Seq Analysis of Infiltrating Neoplastic Cells at the Migrating Front of Human Glioblastoma. *Cell Rep* 2017; 21: 1399-1410.

33 Patel AP, Tirosh I, Trombetta JJ, Shalek AK, Gillespie SM, Wakimoto H *et al*. Single-cell RNA-seq highlights intratumoral heterogeneity in primary glioblastoma. *Science (New York, NY* 2014; 344: 1396-1401.

34 Segerman A, Niklasson M, Haglund C, Bergstrom T, Jarvius M, Xie Y *et al*. Clonal Variation in Drug and Radiation Response among Glioma-Initiating Cells Is Linked to Proneural-Mesenchymal Transition. *Cell Rep* 2016; 17: 2994-3009.

35 Pollak J, Rai KG, Funk CC, Arora S, Lee E, Zhu J *et al*. Ion channel expression patterns in glioblastoma stem cells with functional and therapeutic implications for malignancy. *PloS one* 2017; 12: e0172884.

36 Xie Y, Bergstrom T, Jiang Y, Johansson P, Marinescu VD, Lindberg N *et al*. The Human Glioblastoma Cell Culture Resource: Validated Cell Models Representing All Molecular Subtypes. *EBioMedicine* 2015; 2: 1351-1363.

37 Overman JJ, Clarkson AN, Wanner IB, Overman WT, Eckstein I, Maguire JL *et al*. A role for ephrin-A5 in axonal sprouting, recovery, and activity-dependent plasticity after stroke. *Proceedings of the National Academy of Sciences of the United States of America* 2012; 109: E2230-2239.

38 Petty A, Myshkin E, Qin H, Guo H, Miao H, Tochtrop GP *et al*. A small molecule agonist of EphA2 receptor tyrosine kinase inhibits tumor cell migration in vitro and prostate cancer metastasis in vivo. *PloS one* 2012; 7: e42120.

39 Kaye B, Cussans NJ, Faulkner JK, Stopher DA, Reid JL. The metabolism and kinetics of doxazosin in man, mouse, rat and dog. *Br J Clin Pharmacol* 1986; 21 Suppl 1: 19S-25S.

40 Lin F, de Gooijer MC, Hanekamp D, Brandsma D, Beijnen JH, van Tellingen O. Targeting core (mutated) pathways of high-grade gliomas: challenges of intrinsic resistance and drug efflux. *CNS Oncol* 2013; 2: 271-288.

41 Henrich CJ, Robey RW, Bokesch HR, Bates SE, Shukla S, Ambudkar SV *et al*. New inhibitors of ABCG2 identified by high-throughput screening. *Mol Cancer Ther* 2007; 6: 3271-3278.

42 Robey RW, Honjo Y, Morisaki K, Nadjem TA, Runge S, Risbood M *et al*. Mutations at amino-acid 482 in the ABCG2 gene affect substrate and antagonist specificity. *Br J Cancer* 2003; 89: 1971-1978.

43 Kyprianou N, Benning CM. Suppression of human prostate cancer cell growth by alpha1-adrenoceptor antagonists doxazosin and terazosin via induction of apoptosis. *Cancer research* 2000; 60: 4550-4555.

44 Hu B, Wang Q, Wang YA, Hua S, Sauve CG, Ong D *et al*. Epigenetic Activation of WNT5A Drives Glioblastoma Stem Cell Differentiation and Invasive Growth. *Cell* 2016; 167: 1281-1295 e1218.

45 Verhaak RG, Hoadley KA, Purdom E, Wang V, Qi Y, Wilkerson MD *et al*. Integrated genomic analysis identifies clinically relevant subtypes of glioblastoma characterized by abnormalities in PDGFRA, IDH1, EGFR, and NF1. *Cancer cell* 2010; 17: 98-110.

46 Lisabeth EM, Falivelli G, Pasquale EB. Eph receptor signaling and ephrins. *Cold Spring Harb Perspect Biol* 2013; 5.

47 Gucciardo E, Sugiyama N, Lehti K. Eph- and ephrin-dependent mechanisms in tumor and stem cell dynamics. *Cell Mol Life Sci* 2014; 71: 3685-3710.

48 Day BW, Stringer BW, Boyd AW. Eph receptors as therapeutic targets in glioblastoma. *Br J Cancer* 2014; 111: 1255-1261.

49 Chen J, Ruley HE. An enhancer element in the EphA2 (Eck) gene sufficient for rhombomere-specific expression is activated by HOXA1 and HOXB1 homeobox proteins. *The Journal of biological chemistry* 1998; 273: 24670-24675.

50 Kuang SQ, Bai H, Fang ZH, Lopez G, Yang H, Tong W *et al*. Aberrant DNA methylation and epigenetic inactivation of Eph receptor tyrosine kinases and ephrin ligands in acute lymphoblastic leukemia. *Blood* 2010; 115: 2412-2419.

51 Yu CH, Xu CF, Li YM. Association of MicroRNA-223 expression with hepatic ischemia/reperfusion injury in mice. *Dig Dis Sci* 2009; 54: 2362-2366.

52 Walker-Daniels J, Hess AR, Hendrix MJ, Kinch MS. Differential regulation of EphA2 in normal and malignant cells. *The American journal of pathology* 2003; 162: 1037-1042.

53 Gargiulo G, Cesaroni M, Serresi M, de Vries N, Hulsman D, Bruggeman SW *et al*. In vivo RNAi screen for BMI1 targets identifies TGF-beta/BMP-ER stress pathways as key regulators of neural- and malignant glioma-stem cell homeostasis. *Cancer cell* 2013; 23: 660-676.

54 Yan Y, Wang Q, Yan XL, Zhang Y, Li W, Tang F *et al*. miR-10a controls glioma migration and invasion through regulating epithelial-mesenchymal transition via EphA8. *FEBS letters* 2015; 589: 756-765.

55 Burgold T, Spreafico F, De Santa F, Totaro MG, Prosperini E, Natoli G *et al*. The histone H3 lysine 27-specific demethylase Jmjd3 is required for neural commitment. *PloS one* 2008; 3: e3034.

56 De Santa F, Narang V, Yap ZH, Tusi BK, Burgold T, Austenaa L *et al*. Jmjd3 contributes to the control of gene expression in LPS-activated macrophages. *The EMBO journal* 2009; 28: 3341-3352.

57 Morey L, Aloia L, Cozzuto L, Benitah SA, Di Croce L. RYBP and Cbx7 define specific biological functions of polycomb complexes in mouse embryonic stem cells. *Cell Rep* 2013; 3: 60-69.

58 van den Boom V, Maat H, Geugien M, Rodriguez Lopez A, Sotoca AM, Jaques J *et al*. Non-canonical PRC1.1 Targets Active Genes Independent of H3K27me3 and Is Essential for Leukemogenesis. *Cell Rep* 2016; 14: 332-346.

59 Burgold T, Voituron N, Caganova M, Tripathi PP, Menuet C, Tusi BK *et al*. The H3K27 demethylase JMJD3 is required for maintenance of the embryonic respiratory neuronal network, neonatal breathing, and survival. *Cell Rep* 2012; 2: 1244-1258.

60 Ene CI, Edwards L, Riddick G, Baysan M, Woolard K, Kotliarova S *et al*. Histone demethylase Jumonji D3 (JMJD3) as a tumor suppressor by regulating p53 protein nuclear stabilization. *PloS one* 2012; 7: e51407.

61 Danussi C, Akavia UD, Niola F, Jovic A, Lasorella A, Pe'er D *et al*. RHPN2 drives mesenchymal transformation in malignant glioma by triggering RhoA activation. *Cancer research* (Research Support, N.I.H., Extramural

Research Support, Non-U.S. Gov't

Research Support, U.S. Gov't, P.H.S.) 2013; 73: 5140-5150.

62 Frattini V, Trifonov V, Chan JM, Castano A, Lia M, Abate F *et al*. The integrated landscape of driver genomic alterations in glioblastoma. *Nature genetics* 2013; 45: 1141-1149.

63 Hashizume R, Andor N, Ihara Y, Lerner R, Gan H, Chen X *et al*. Pharmacologic inhibition of histone demethylation as a therapy for pediatric brainstem glioma. *Nature medicine* 2014; 20: 1394-1396.

64 Li JJ, Liu DP, Liu GT, Xie D. EphrinA5 acts as a tumor suppressor in glioma by negative regulation of epidermal growth factor receptor. *Oncogene* 2009; 28: 1759-1768.

65 Boyd AW, Bartlett PF, Lackmann M. Therapeutic targeting of EPH receptors and their ligands. *Nat Rev Drug Discov* 2014; 13: 39-62.

66 Ferluga S, Tome CM, Herpai DM, D'Agostino R, Debinski W. Simultaneous targeting of Eph receptors in glioblastoma. *Oncotarget* 2016; 7: 59860-59876.

Figure legends

Figure 1. Genome-wide analysis of genes and pathway deregulated in mGIC.

(A) Schematic of the experimental setup (non-neoplastic NSC and NSC Bmi1^{Over} as well as neoplastic mGIC). (B) Average profile for H3K27me3 across the three studied genotypes – mGIC, NSC Bmi1^{Over} and NSC – within 5 kb of the TSS. Scores associated with significantly called peaks in mGIC are plotted over the genomic regions of the three genotypes, centred at the TSS. (C) Heatmap for H3K27me3 across the three studied genotypes – mGIC, NSC Bmi1^{Over} and NSC. Scores associated with significantly called peaks in mGIC (top panels, cluster A) and in NSC (bottom panels, cluster B) are plotted over the genomic regions of the three genotypes, centred at the TSS. (D) Heatmap of relative expression of genes deregulated in mGIC across the three studied genotypes – mGIC, NSC Bmi1^{Over} and NSC. (E) Venn diagram showing genes uniquely or commonly repressed in the comparisons mGIC vs NSC Bmi1^{Over} and mGIC vs NSC. (F) Proportion of commonly repressed genes in mGIC concomitantly enriched for H3K27me3 (mGIC unique concordant) is shown in blue. (G) qPCR showing the expression levels of a selection of deregulated genes in biologically independent replicas of NSC, NSC Bmi1^{Over} and mGIC (n=3). *, $p < 0.05$; **, $p < 0.01$; ***, $p < 0.001$, error bars represent ± SEM. (H) IPA analysis identifying canonical pathways specifically and significantly enriched for H3K27me3 in mGIC compared to hGIC of a publicly available dataset (numbers indicate –log(p value) and threshold for significance is 1.3; red indicates significantly higher levels of H3K27me3 and white indicates lower).

Figure 2. Assessment of Bmi1-dependency of deregulated genes.

(A) Western blot (left) and quantification (right) showing effective Bmi1 silencing in shBmi1 mGIC compared to the control shScr (n=4). (B) qPCR analysis of Bmi1-dependency of candidate gene expression (n=3). (C) Visualisation of the EfnA5 locus, centred on the TSS, shows a differential H3K27me3 distribution (green) and expression (blue) between mGIC and the non-neoplastic NSC and NSC $Bmi1^{Over}$. (D) Schematic representation of the EfnA5 region where PS 3.2 and PS 3.5 primer pairs allign (top), and quantification of qChIP assay (bottom) confirms that the H3K27me3 levels depend on Bmi1 expression in mGIC. Immunoprecipitated chromatin (mock) was used as negative control (n=6). *, $p < 0.05$; **, $p < 0.01$; ***, $p < 0.001$; ****, $p < 0.0001$; error bars represent ± SEM.

Figure 3. Bmi1 controls the H3K27me3-dependent repression of EfnA5 through downregulation of JmjD3.

(A) High resolution images showing shScr cells overexpressing mCherry-JmjD3: the H3K27me3 PLA signal at EfnA5 locus is detectable in mCherry- cell (left panel) and not in mCherry+ cell (right panel). (B) Representative images of the PLA assay in shScr and shBmi1 mGIC in combination with JmjD3 reconstitution and Ezh2 inhibitor treatment (Ezh2i). (C) and (D) Quantification of the percentage of PLA positive nuclei with EfnA5 probe (C), or negative probe (D), showing the specific modulation of the H3K27me3 levels at *EfnA5* locus (n=6). *, $p < 0.05$; **, $p < 0.01$; ***, $p < 0.001$; ****, $p < 0.0001$; error bars represent ± SEM. Scale bars represent 20 µm in (A) and 50 µm in (C).

Figure 4. EfnA5 signalling negatively regulates mGIC properties *in vitro*.

(A) Immunocytochemistry for phalloidin (green) and corresponding quantification show that stress fibres increase in shScr upon activation of EfnA5 signalling similarly to shBmi1 (n=3). (B) Immunocytochemistry for GFAP (yellow) and quantification reveal increased cellular processes lengh in mGIC with high levels of EfnA5 (n=3), yellow arrowheads indicate pronounced cellular processes. (C) Representative pictures and quantitative analysis of the proliferation rate upon prolonged treatment with mouse recombinant EfnA5 or Fc control. The yellow mask represents the % of confluence (n=9). (D) Representative pictures and quantitative analysis at different time points after creation of wound and upon prolonged treatment with mouse recombinant EfnA5 or Fc control. Yellow mask represents the % confluence and quantification show the migration rate over time (n=6). *, $p < 0.05$; **, $p < 0.01$; ***, $p < 0.001$; ****, $p < 0.0001$; error bars represent ± SEM. Scale bars represent 50 µm in (A,B) and 800 µm in (C,D).

Figure 5. EfnA5 silencing rescues Bmi1kd mGIC properties.

(A) Immunocytochemistry and corresponding quantification for phalloidin (green) and Nestin (magenta) shows that the increase of stress fibres and cellular processes length depends on the upregulation of EfnA5. Endogenous mCherry is shown in red (n=3). (B) Quantitative analysis of the proliferation rate showing that Bmi1 promotes mGIC proliferation by repressing EfnA5. (n=6). (C) Quantification of the migration rate reveals that high EfnA5 expression inhibits the migratory capacity of mGIC (n=6). *, $p < 0.05$; **, $p < 0.01$; ***, $p < 0.001$; ****, $p < 0.0001$; error bars represent ± SEM. Scale bars represent 50 µm in (A) and 100 µm in (B).

Figure 6. EfnA5 repression mediates Bmi1 modulated tumour development in an allograft model.

(A) Tumour incidence was monitored over a representative number of time points with BLI (shScr and shBmi1 n=9; shBmi1+shmCherry and shBmi1+shEfnA5 n=8). (B) Representative BLI images of NODSCID mice 54 days post-injection of mGIC with different expression levels of EfnA5 and corresponding (B) frequency distribution plot (shScr and shBmi1 n=9; shBmi1+shmCherry and shBmi1+shEfnA5 n=8). (C) Histology of representative tumour areas, H&E shows pleomorphic glial cells with compacted tumour growth with necrosis; IHC shows tumour cells are strongly positive for GFAP, Olig2 and Sox2, confirming their glial origin. Scale bar = 250µm.

Figure 7. EFNA5 mediates BMI1 function in hGIC.

(A) Contingency tables for the expression levels of BMI1 and EFNA5 in GBM cells from single-cell RNAseq datasets (example table top left); levels of significance of negative association using both Fisher's exact test and Barnard's test are in parenthesis. (B-D) Scatter plots with linear regression statistics showing the correlation between levels of BMI1 and EFNA5 for two hGIC datasets GSE89399 (B) and GSE89623 (C), and for microarray data from hGIC of the Proneural subgroup from the HGCC (D). (E) Levels of BMI1 and EFNA5 by Western blot for the two hGIC lines, U3033 and U3118, after BMI1 knockdown, GAPDH was used as a control. (F) Immunofluorescence staining in U3118 cells for phosphorylated EphA receptors 2, 3 and 4 is shown in after BMI1 knockdown and EFNA5 pathway inhibition with recombinant protein (n=3). (G) Representative images and quantification for EdU staining in U3118 cells after BMI1 knockdown and EFNA5 pathway inhibition, showing an increase in downstream pathway activation in the condition with highest EFNA5 expression and no EFNA5 pathway blockade (n=3). (H) Proliferation assays for U3118 after BMI1 knockdown with shRNA (upper) and concomitant BMI1 knockdown and EFNA5 pathway inhibition with recombinant proteins (lower) (n=3). *, $p < 0.05$; **, $p < 0.01$; ***, $p < 0.001$; ****, $p < 0.0001$; error bars represent ± SEM. Scale bar is 250µm (F,G).

Figure 8. Doxazosin effectively targets BMI1^{high}/EFNA5^{low} hGIC *in vitro* and *in vivo*.

(A) U3118shScr (black) and U3118shBMI1 (green) cells were both treated with either vehicle control or doxazosin (DOX) 5µM and counted at selected time-points (n=3). (B) At day 8, the number of U3118shScr DOX treated cells, as a fraction of U3118shScr vehicle treated cells, was significantly less than the number of U3118shBMI1 Dox treated cells as a fraction of U3118shBMI1 vehicle treated cells (n=3). (C+D) Western blot (C) and quantitative analysis (D) showing the levels of EphA2-4, phosphorylated EphA2-4, ERK1/2 and phosphorylated ERK1/2 for the same conditions as in (A) (n=3). (E) Histology of representative tumour areas with human Vimentin immunohistochemistry, H&E and Ki67; scale bars are 1mm for hVIM and 50µm for H&E and Ki67 (n=8). (F) Tumour volume assessed by automated quantification of human vimentin immunohistochemistry. (G) Tumour proliferation assessed by Ki67 count per high power field (HPF). *, $p < 0.05$; **, $p < 0.01$; ***, $p < 0.001$; ****, $p < 0.0001$; error bars represent SEM.

Ricci et al. Figure 1

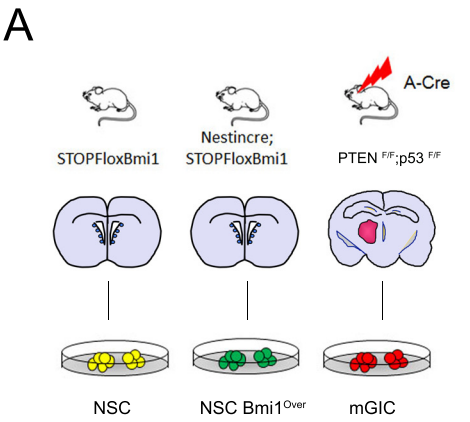

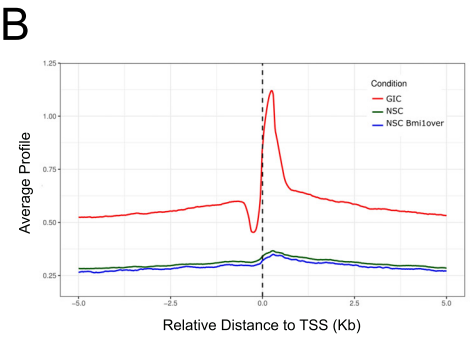

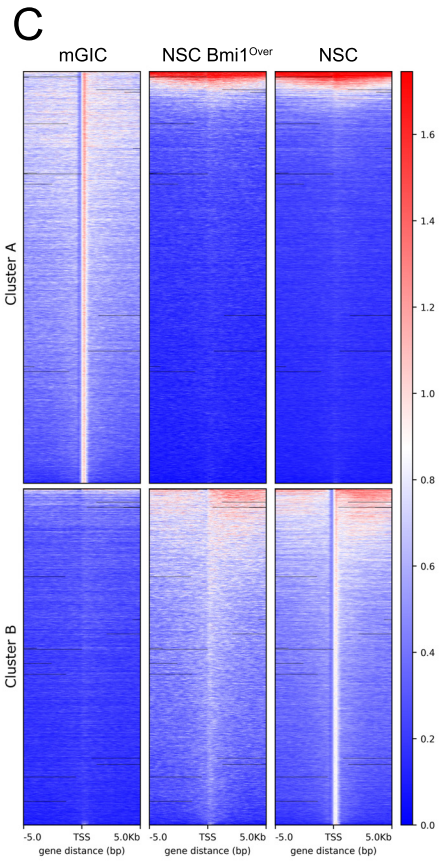

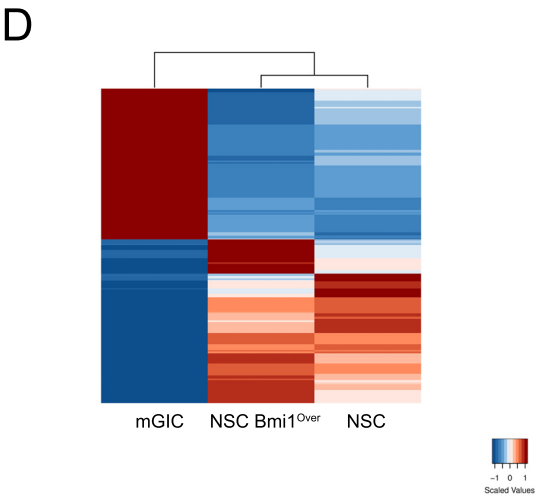

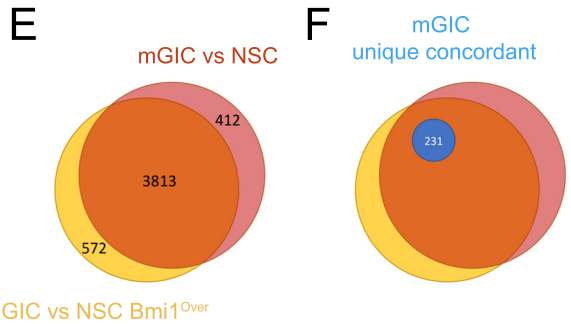

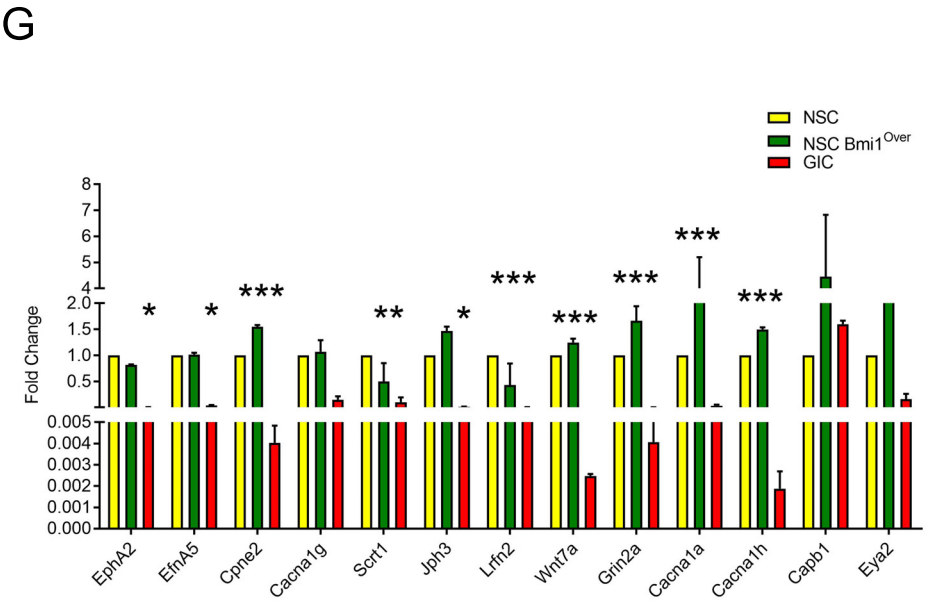

H

Ingenuity Pathways	Unique GIC peaks	Unique GIC peaks shared with hGIC
Neuropathic Pain Signaling In Dorsal Horn Neurons	3.19	5.34
Complement System	3.16	4.68
GPCR-Mediated Nutrient Sensing in Enteroendocrine Cells	2.96	6.34
Cellular Effects of Sildenafil (Viagra)	2.82	4.26
CREB Signaling in Neurons	2.76	5.24
Axonal Guidance Signaling	2.73	7.14
Citrulline-Nitric Oxide Cycle	2.68	2.26
GABA Receptor Signaling	2.44	4.05
Dopamine-DARPP32 Feedback in cAMP Signaling	2.38	5.13
Neuroprotective Role of THOP1 in Alzheimer's Disease	2.23	1.71
Glucocorticoid Receptor Signaling	2.22	3.99
Type II Diabetes Mellitus Signaling	2.22	1.92
Sphingosine-1-phosphate Signaling	2.1	3.04
Phagosome Formation	2.1	2.53
PKCθ Signaling in T Lymphocytes	2.02	2.22
Superpathway of Citrulline Metabolism	1.95	2.29
Gαi Signaling	1.81	2.55
Synaptic Long Term Potentiation	1.7	3.71
G-Protein Coupled Receptor Signaling	1.66	3.76
Corticotropin Releasing Hormone Signaling	1.62	4.49
GPCR-Mediated Integration of Enteroendocrine Signaling Exemplified by an L Cell	1.57	3.48
Endocannabinoid Cancer Inhibition Pathway	1.54	2.31
Glioblastoma Multiforme Signaling	1.53	2.57
Leukocyte Extravasation Signaling	1.52	3.26
Calcium Signaling	1.5	2.97
Serotonin and Melatonin Biosynthesis	1.48	2.26
nNOS Signaling in Skeletal Muscle Cells	1.47	3.44
Opioid Signaling Pathway	1.45	2.67
Amyotrophic Lateral Sclerosis Signaling	1.4	1.73
Circadian Rhythm Signaling	1.36	1.35
Role of Wnt/GSK-3β Signaling in the Pathogenesis of Influenza	1.35	1.5
Eicosanoid Signaling	1.35	2.29
cAMP-mediated signaling	1.32	3.94

Ricci et al. Figure 2

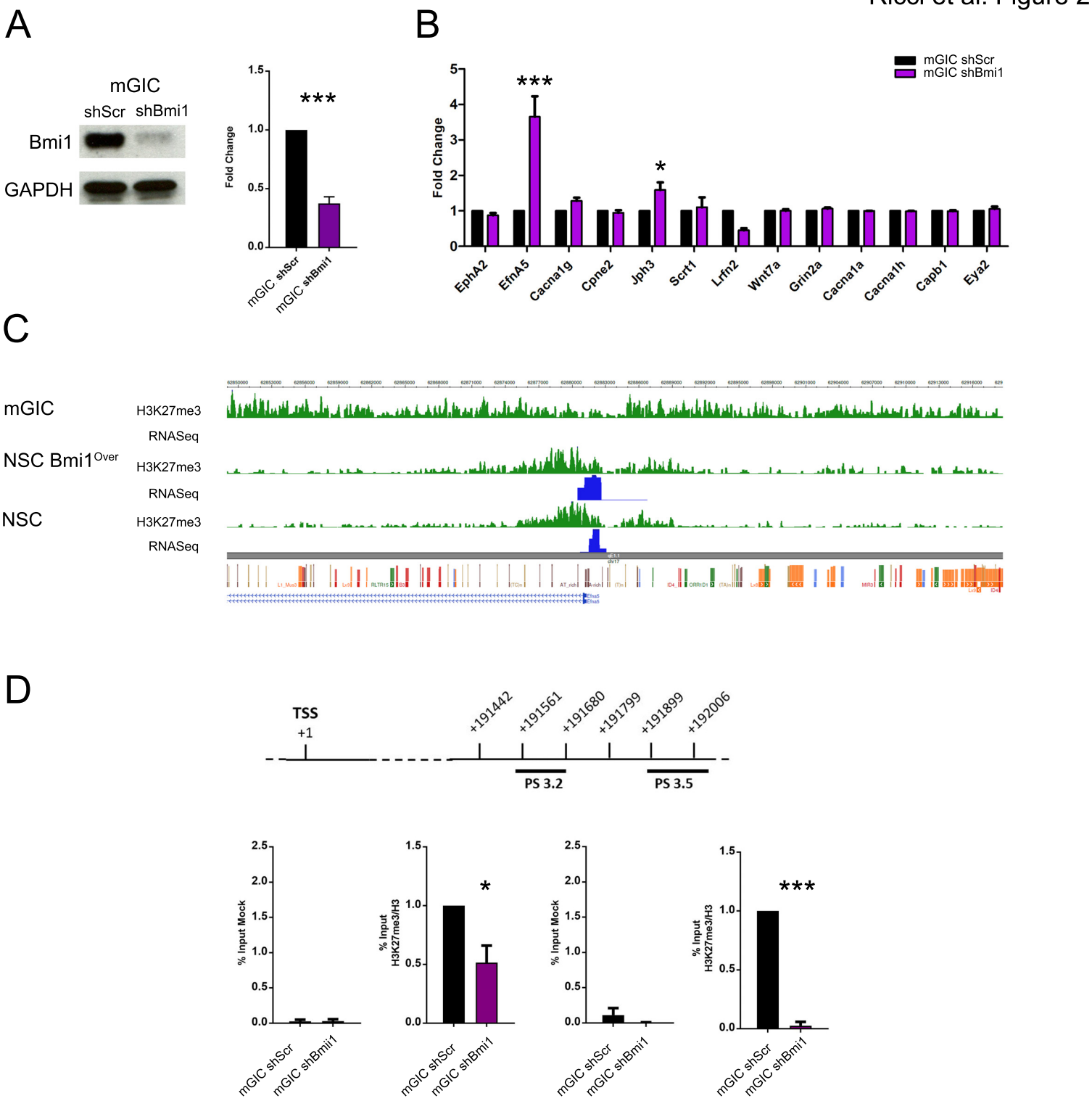

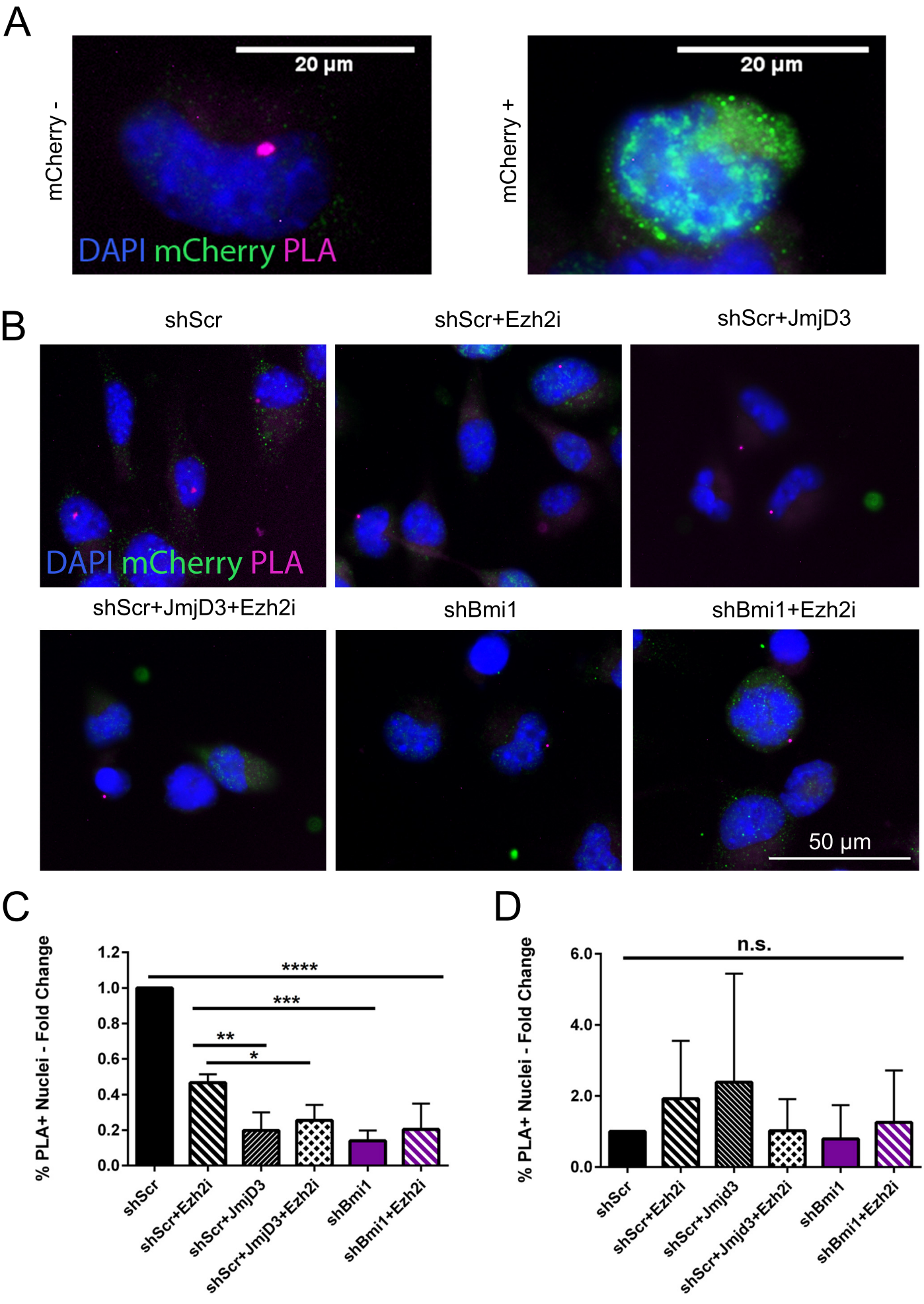
A
mCherry -
20 µm
DAPI mCherry PLA
mCherry +
20 µm
B
shScr
shScr+Ezh2i
shScr+JmjD3
DAPI mCherry PLA
shScr+JmjD3+Ezh2i
shBmi1
shBmi1+Ezh2i
50 µm
C
% PLA+ Nuclei - Fold Change
1.2
1.0
0.8
0.6
0.4
0.2
0.0
****
***
**
*
shScr
shScr+Ezh2i
shScr+JmjD3
shScr+JmjD3+Ezh2i
shBmi1
shBmi1+Ezh2i
D
% PLA+ Nuclei - Fold Change
6.0
4.0
2.0
0.0
n.s.
shScr
shScr+Ezh2i
shScr+Jmjd3
shScr+Jmjd3+Ezh2i
shBmi1
shBmi1+Ezh2i

Ricci et al. Figure 4

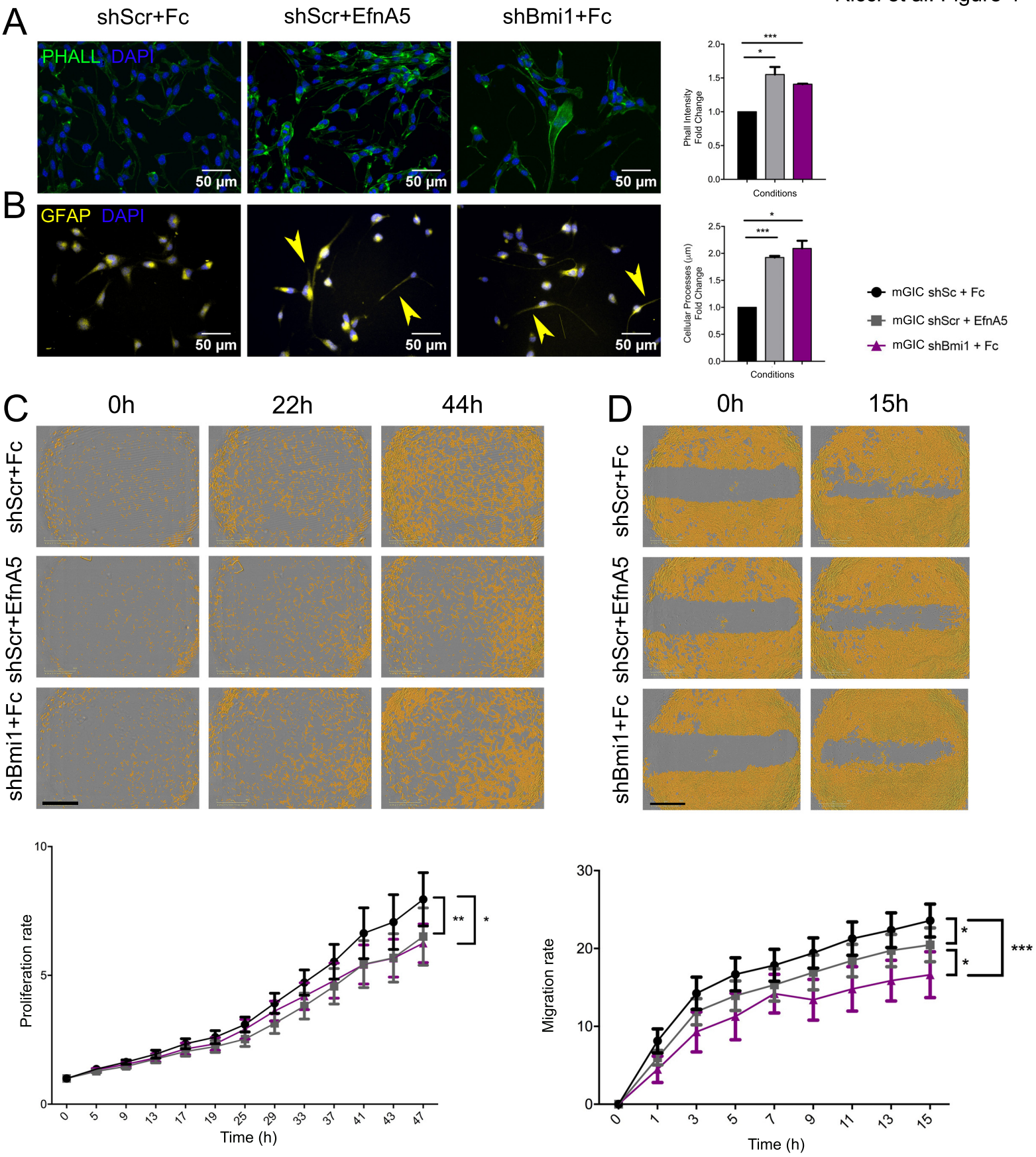

Ricci et al. Figure 5

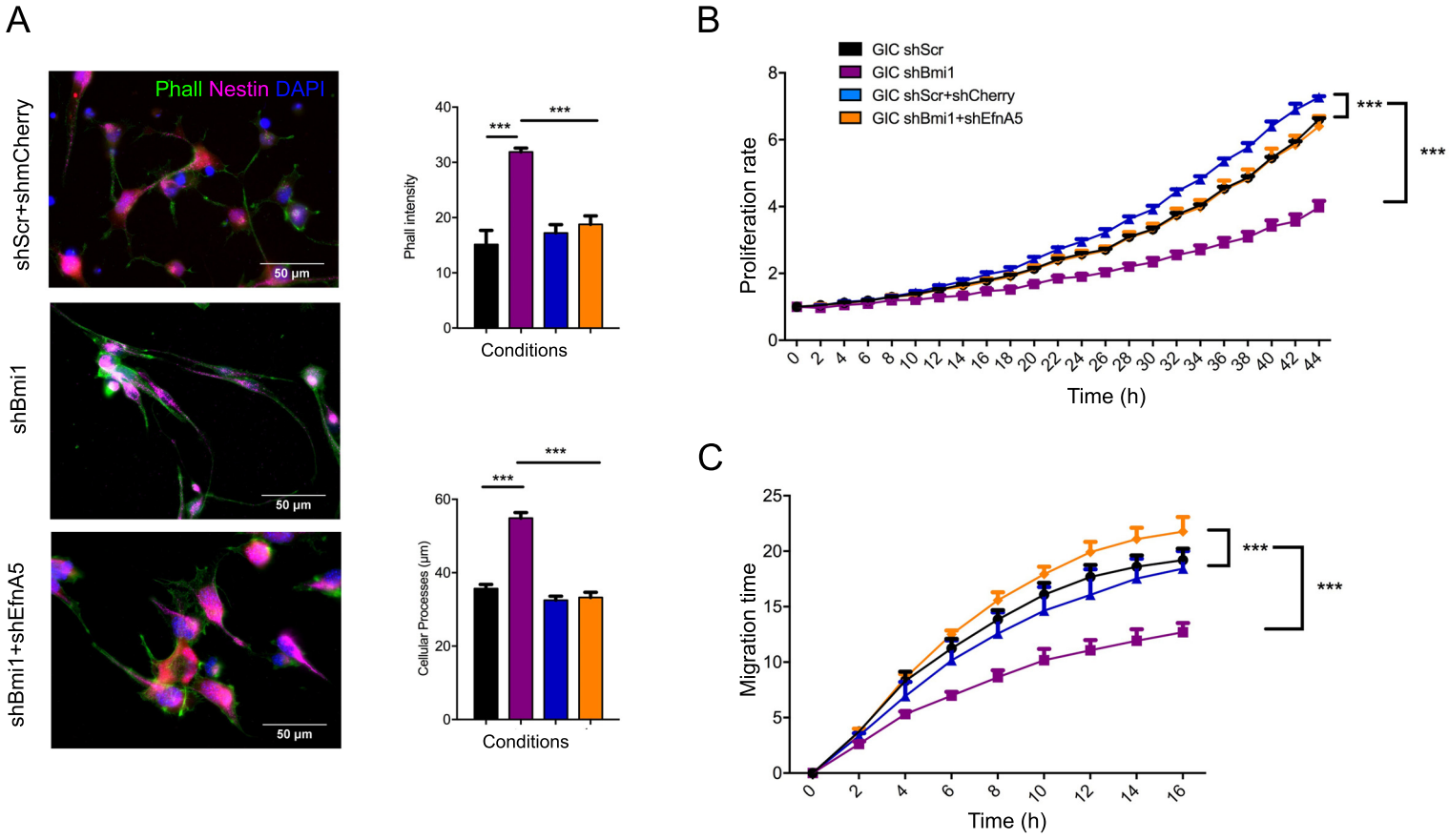

Ricci et al. Figure 6

A

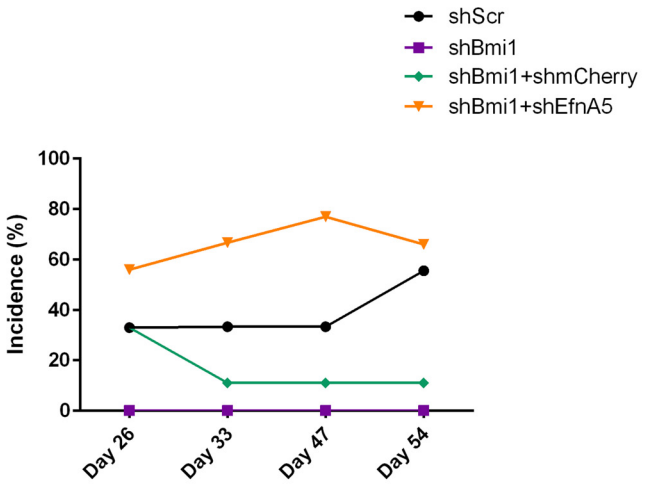

shScr vs. shBmi1	38.80	22.80 to 54.79	Yes	***
shBmi1 vs. shBmi1+shEfnA5	-66.43	-82.42 to -50.43	Yes	****
shBmi1+shmCherry vs. shBmi1+shEfnA5	-49.93	-65.92 to -33.93	Yes	****

B

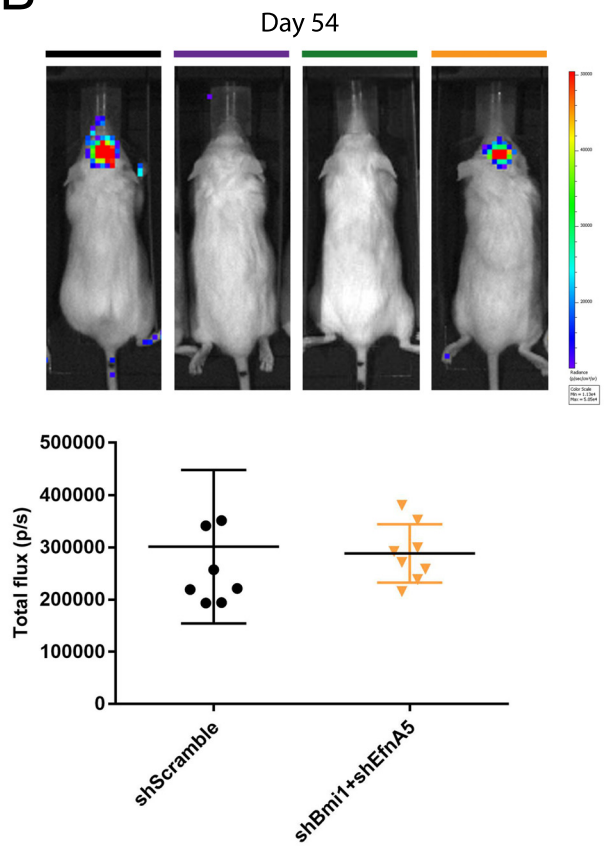

C

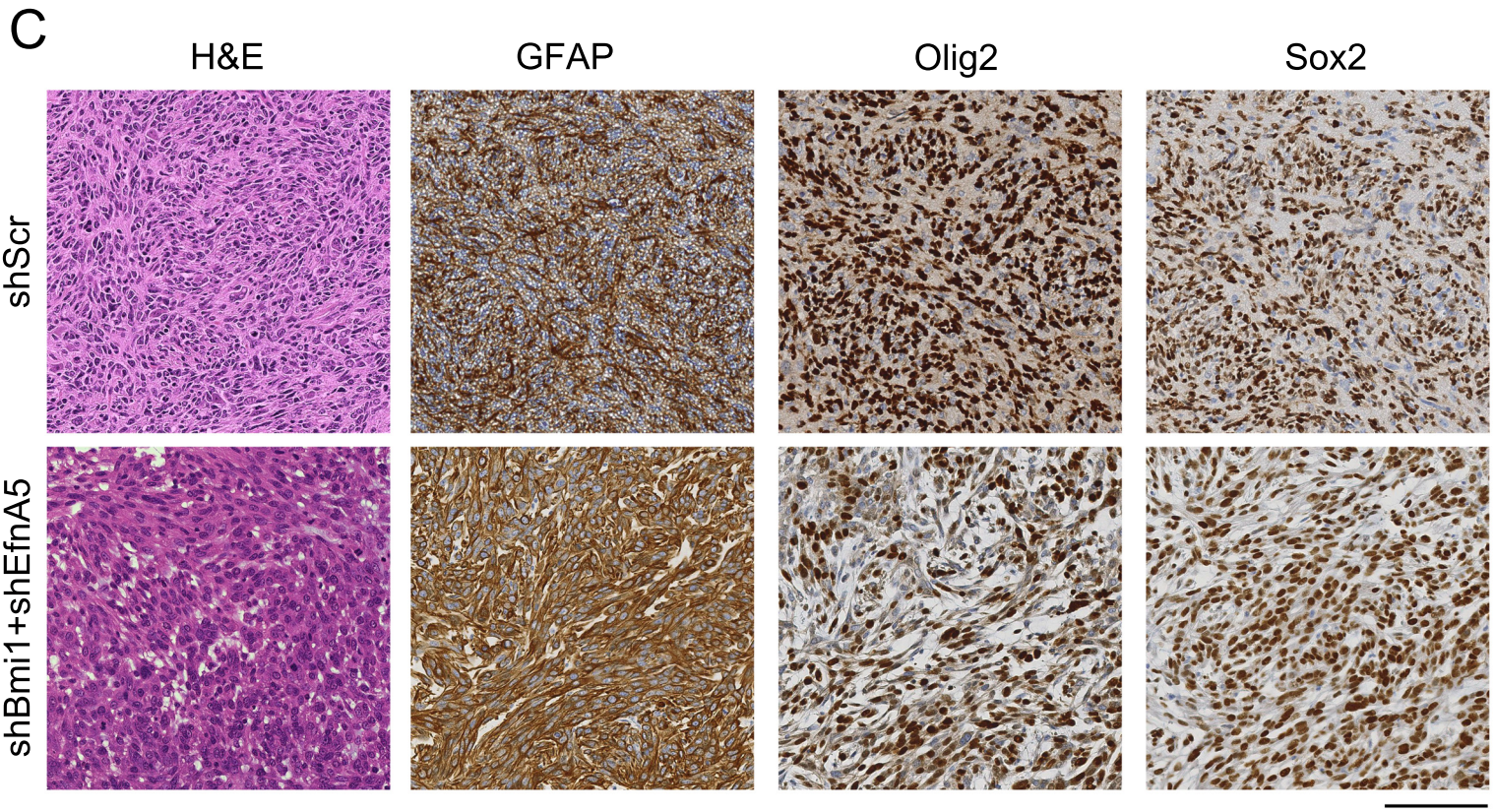

A

Legend

EFNA5 / BMI1	Low	High
Low		BMI1^{low}, EFNA5^{high}
High	BMI1^{high}, EFNA5^{low}	

GBMSeq, Darmanis et al. 2017, All neoplastic cells (***)

EFNA5 / BMI1	Low	High
Low	33	92
High	21	1

GSE57872, Patel et al. 2014 (***)

EFNA5 / BMI1	Low	High
Low	7	75
High	134	110

B

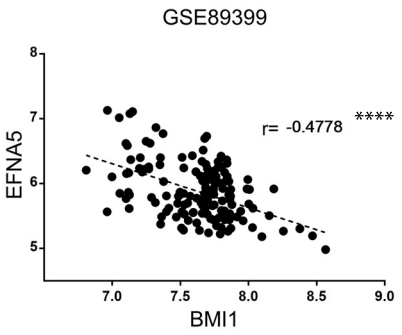

C

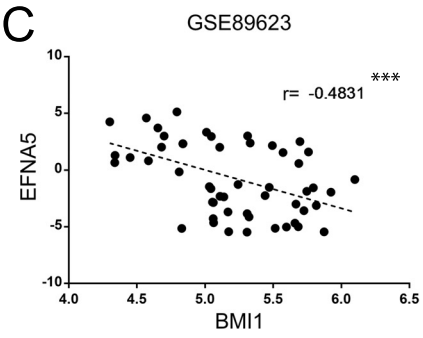

D

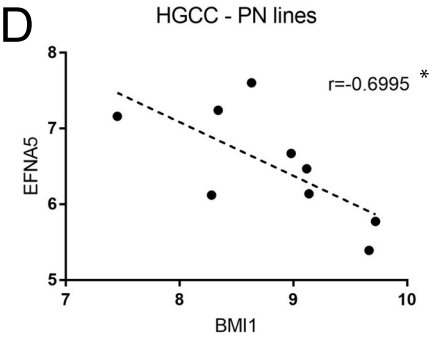

E

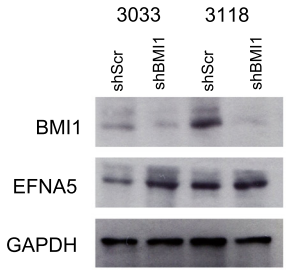

F

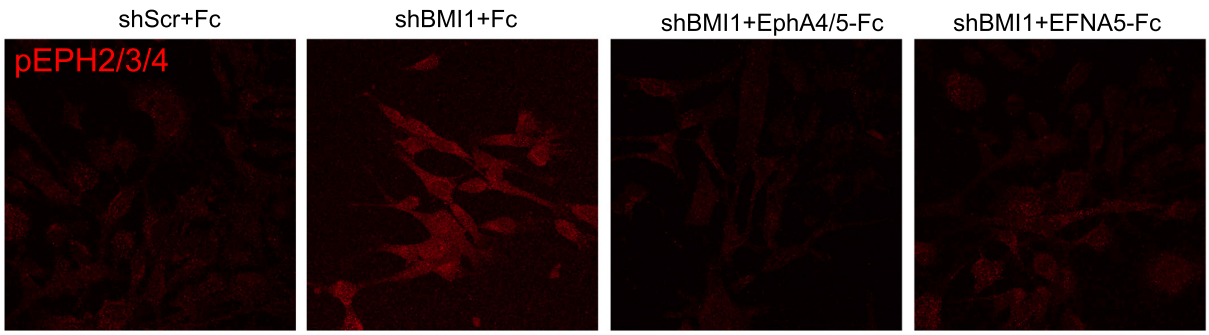

G

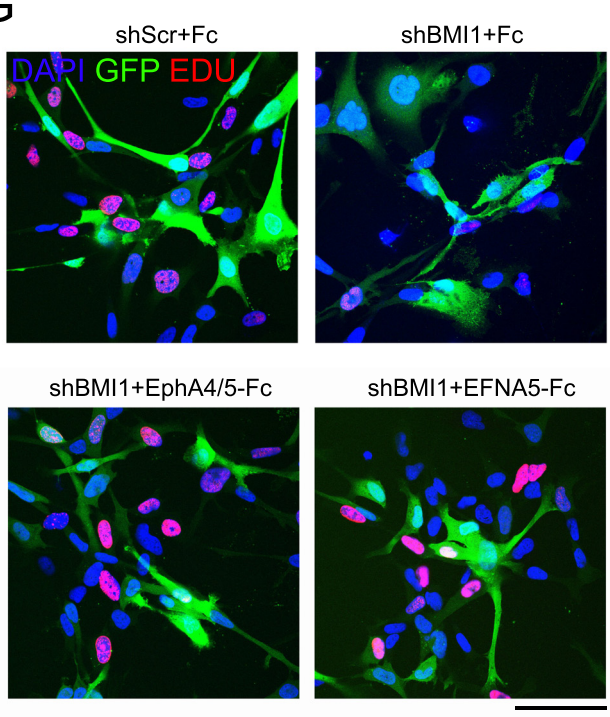

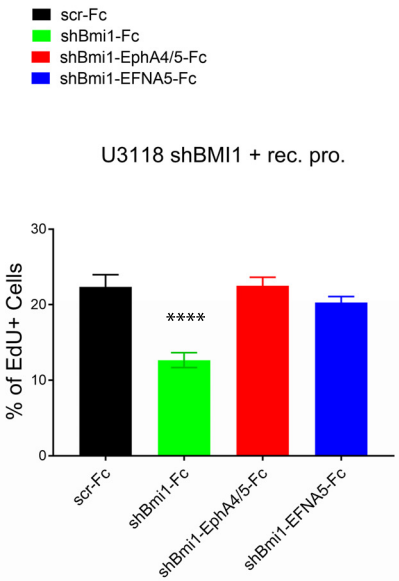

H

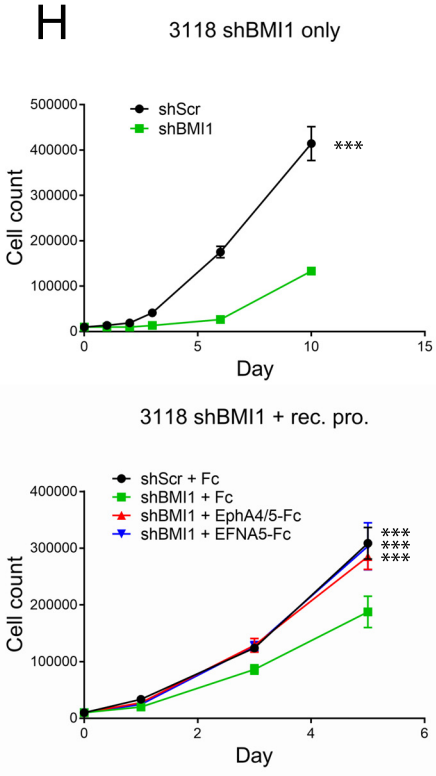

Ricci et al. Figure 8

A

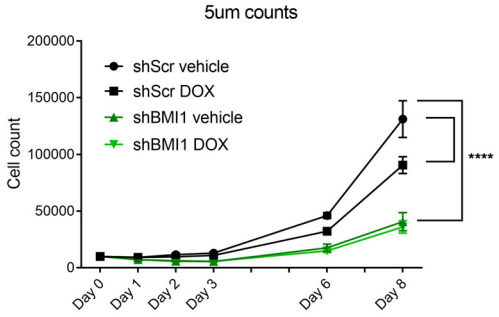

Day 8	Significance
shScr vehicle vs. shScr DOX	****
shScr vehicle vs. shBMI1 vehicle	****
shScr vehicle vs. shBMI1 DOX	****
shScr DOX vs. shBMI1 vehicle	****
shScr DOX vs. shBMI1 DOX	****
shBMI1 vehicle vs. shBMI1 DOX	**ns**

B

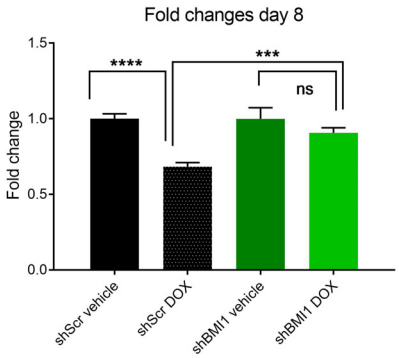

C

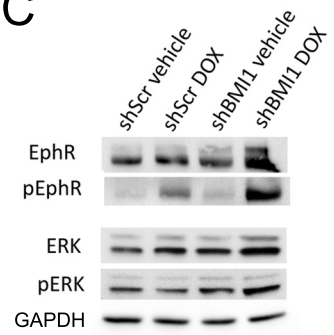

D

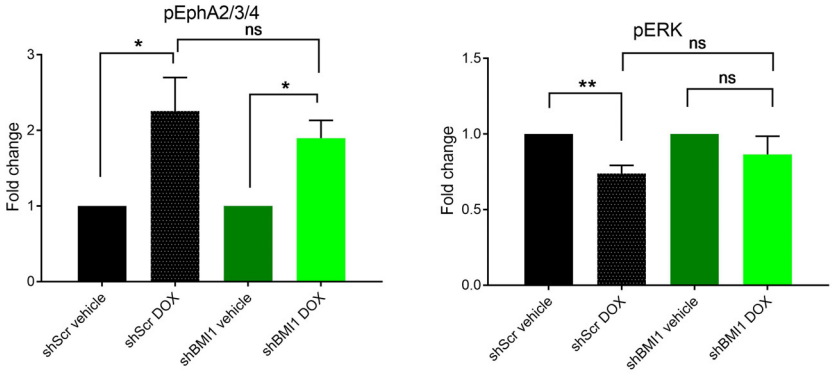

E

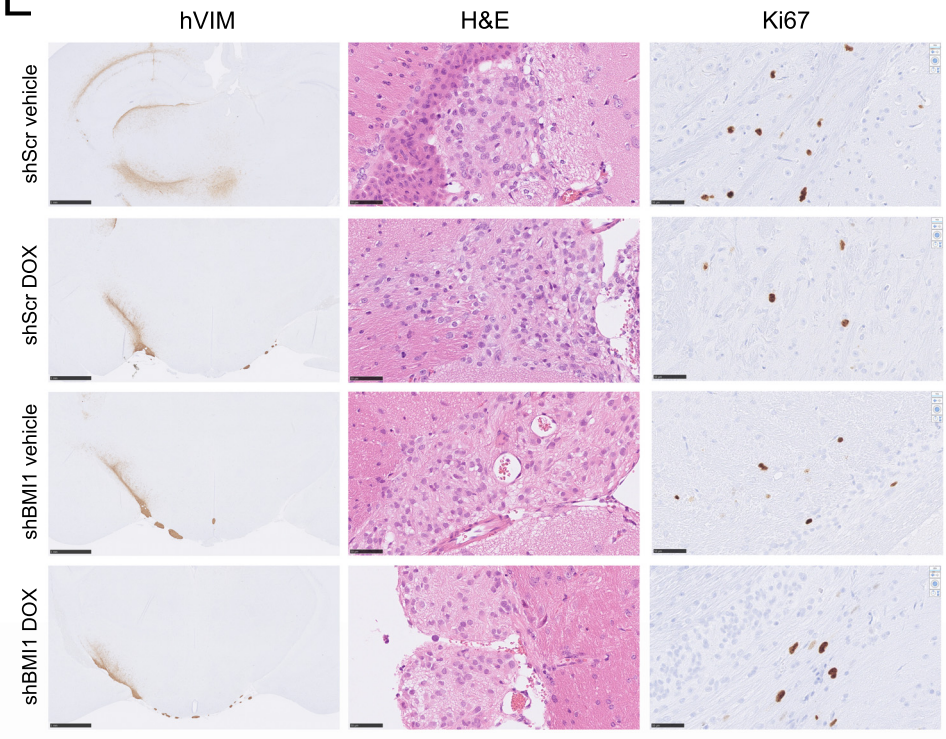

F

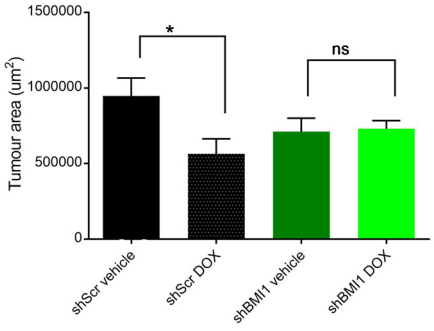

G

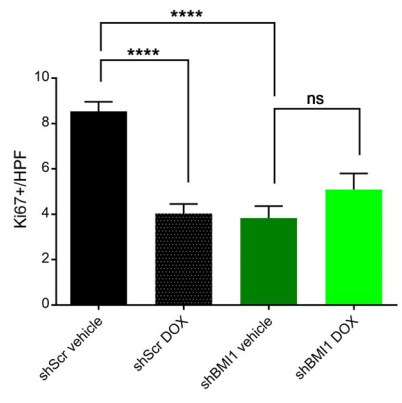

Supplementary Figure Legends

Figure S1. **Validation of deregulated target genes identified in the genome-wide analysis.**

(A) IPA comparative analysis identifying canonical pathways specifically and significantly enriched for H3K27me3 in GIC and NSC Bmi1^{Over}. Numbers indicate –log(p-value), threshold for significance is 1.3. (B) Table showing overlap between unique concordant genes in the mGIC context and cell lines in the NIH Roadmap Epigenomics database (H3K27me3 datasets); significance is reported taking account of p-values adjusted for FDR (< 0.05). (C) Venn diagram showing the overlap between unique concordant genes in the mGIC context and a publicly available H3K27me3 hGIC dataset.

Figure S2. Bmi1 represses the expression of EfnA5 but not of cell cycle inhibitors in mGIC.

(A) Western blot and corresponding quantitive analysis showing increase EfnA5 expression in mGIC upon Bmi1 silencing as compared to control shScr (n=3). (B) Visualisation of the whole EFNA5 locus shows a differential H3K27me3 distribution (green) between hGIC (here named GSC as in Rheinbay 2013) and human NSC. (C) RNA microarray expression data for BMI1 and EFNA5 levels in hGIC and human NSC for the same cells shown in (B). (D) qPCR reveals no significant up-regulation of the expression the cell cycle inhibitors $p16^{Ink4A}$, $p19^{Arf}$ and $p21^{Cip1/Waf1}$ in shBmi1 mGIC compared to the control (n=6). ***, $p < 0.001$; error bars represent ± SEM.

Figure S3. Schematic representation of Proximity Ligation Assay (PLA).

(A) Two primary antibodies (black) are used to recognise EfnA5 biotinylated probe (red) and H3K27me3 (green) at the *EfnA5* locus. Secondary antibodies (blue) enable detection of the PLA signal after ligation and amplification of conjugated oligonucleotide sequences (pink). (B) Model of the PcG-mediated regulation of EfnA5 locus. Schematic showing the proposed PcG-dependent mechanism regulating the expression of EfnA5 in GIC (upper panel) and NSC (lower panel) integrated within the existing knowledge of EfnA5 regulation in normal and neoplastic NSC.

Figure S4. EfnA5 silencing rescues proliferation and migration in shBmi1 mGIC.

(A) Western blot and corresponding quantitive analysis showing the levels of Bmi1 and EfnA5 in mGIC transduced with different combinations of shRNAs (n=2). (B) Representative pictures of the proliferation rate at different time points upon Bmi1 and/or EfnA5 silencing. The yellow mask represents the % of confluence (scale bar = 800µm). (C) Representative images of the gap closure assay. The yellow mask represents the % of confluence (scale bar = 800µm). (D) Representative pictures of neurosphere formation assay with corresponding quantification. The number of the neurospheres in shBmi1 condition is increased when EfnA5 expression is silenced (scale bar = 400 µm; n=3). *, $p < 0.05$; **, $p < 0.01$; ***, $p < 0.001$; ****, $p < 0.0001$; error bars represent ± SEM.

Figure S5: EfnA5 mediates the reduced invasion of mGIC induced by Bmi1 silencing.

(A) Representative micrographs of neurospheres with corresponding quantification from a neurosphere formation assay. The size of neurospheres is decreased in conditions with higher EfnA5 (n=3). (B) Quantitative analysis of invasion assay showing the percentage of invading nuclei at distances 0-120µm form the bottom of a collagen gel, showing that mGIC expressing high levels of EfnA5 partially lose their invasive potential. NSC represent the negative control (n=6). *, $p < 0.05$; **, $p < 0.01$; ***, $p < 0.001$; ****, $p < 0.0001$; error bars represent ± SEM.

Figure S6. mGIC overexpressing Bmi1 show tumourigenic features.

(A) Western blot and corresponding quantitive analysis showing the levels of Bmi1 and EfnA5 in mGIC transduced with different combinations of shRNAs (n=2). *, $p < .05$; **, $p < .01$, error bars represent ± SEM. (B) Histology of representative tumour areas arising from allografted shScr GIC with diffuse infiltration patter and strong positivity for GFP. Scale bar = 1 mm (top panel) and 250 μm (middle and bottom panel).

Figure S7. EFNA5 mediates BMI1 function in hGIC.

(A) Scatter plot with linear regression statistics showing the correlation between levels of BMI1 and EFNA5 for microarray data from TCGA (hthgu133a). (B) A schematic showing the method used for identifying cells with high and low expression of BMI1 and EFNA5 in the single-cell RNAseq datasets: red identifies cells with a $BMI1^{low}EFNA5^{high}$ profile and blue identifies cells with the inverse $BMI1^{high}EFNA5^{low}$ profile. (C) Representative images and quantification for EdU staining in U3033 cells after BMI1 knockdown and EFNA5 pathway inhibition. (D) Proliferation assays for U3033 after BMI1 knockdown with shRNA (upper) and concomitant BMI1 knockdown and EFNA5 pathway inhibition with recombinant proteins (lower). *, $p < 0.05$; **, $p < 0.01$; ***, $p < 0.001$; ****, $p < 0.0001$; error bars represent ± SEM. Scale bar =250 μm.

Figure S8. Doxazosin effectively targets BMI1^{high}/EFNA5^{low} hGIC *in vitro* and *in vivo*.

(A) Doxazosin levels in the serum and brain homogenate of experimental mice over 24 hours after 50mg/kg subcutaneous injection (one mouse injected at each time-point). (B) Doxazosin levels in the serum and brain homogenate after concomitant administration of elacridar (Elac), Cnt+dose1 – vehicle control + 50mg/kg doxazosin, Cnt+dose2 – vehicle control + 100mg/kg doxazosin, Elac+dose1 – 100mg/kg + 50mg/kg doxazosin, Elac+dose2 – 100mg/kg elacridar + 100mg/kg doxazosin (n=2); *, $p < 0.05$; **, $p < 0.01$; ***, $p < 0.001$; ****, $p < 0.0001$; error bars represent SEM. (C) Treatment regime for in vivo co-administration of doxazosin (blue bars) and elacridar (red bars). Elacridar given orally four hours prior to subcutaneous doxazosin dose. (D) Histology of representative tumour areas with H&E and GFAP, OLIG2, SOX2 and human Vimentin; scale bars represent 2.5mm for human vimentin (low mag.), and 50µm for all others.

Ricci et al. Figure S1

A

Ingenuity Pathways	Unique GIC peaks	Unique NSC Bmi1over peaks
Neuropathic Pain Signaling In Dorsal Horn Neurons	3.19	0.79
Complement System	3.16	0.25
GPCR-Mediated Nutrient Sensing in Enteroendocrine Cells	2.96	0.53
Cellular Effects of Sildenafil (Viagra)	2.82	0.7
CREB Signaling in Neurons	2.76	0.53
Axonal Guidance Signaling	2.73	0.82
Citrulline-Nitric Oxide Cycle	2.68	
GABA Receptor Signaling	2.44	0.4
Dopamine-DARPP32 Feedback in cAMP Signaling	2.38	0
Neuroprotective Role of THOP1 in Alzheimer's Disease	2.23	0
Glucocorticoid Receptor Signaling	2.22	0
Type II Diabetes Mellitus Signaling	2.22	0.47
Sphingosine-1-phosphate Signaling	2.1	0
Phagosome Formation	2.1	0.72
PKCθ Signaling in T Lymphocytes	2.02	0.43
Sphingomyelin Metabolism	1.99	
L-cysteine Degradation III	1.96	
Thiosulfate Disproportionation III (Rhodanese)	1.96	
Glutamate Degradation II	1.96	
Aspartate Biosynthesis	1.96	
Superpathway of Citrulline Metabolism	1.95	0.5
Gαi Signaling	1.81	0
Synaptic Long Term Potentiation	1.7	1.07
L-cysteine Degradation I	1.68	
G-Protein Coupled Receptor Signaling	1.66	0.26
Corticotropin Releasing Hormone Signaling	1.62	0.57
GPCR-Mediated Integration of Enteroendocrine Signaling Exemplified by an L Cell	1.57	0.28
Endocannabinoid Cancer Inhibition Pathway	1.54	0
Glioblastoma Multiforme Signaling	1.53	0.39
Leukocyte Extravasation Signaling	1.52	0
Calcium Signaling	1.5	0
Ephrin A Signaling	1.49	0
Serotonin and Melatonin Biosynthesis	1.48	
nNOS Signaling in Skeletal Muscle Cells	1.47	0.58
Opioid Signaling Pathway	1.45	0.85
Amyotrophic Lateral Sclerosis Signaling	1.4	0.52
Th1 Pathway	1.38	0.42
Th2 Pathway	1.37	0
IL-17A Signaling in Airway Cells	1.37	0.24
Circadian Rhythm Signaling	1.36	
Role of Wnt/GSK-3β Signaling in the Pathogenesis of Influenza	1.35	0
Eicosanoid Signaling	1.35	0.31
cAMP-mediated signaling	1.32	0
Atherosclerosis Signaling	1.3	0
Guanine and Guanosine Salvage I		1.31
Melanocyte Development and Pigmentation Signaling	0.34	1.33
DNA Double-Strand Break Repair by Homologous Recombination		1.33
Dermatan Sulfate Biosynthesis	0	1.39
Dopamine Degradation		1.41
Agrin Interactions at Neuromuscular Junction	0.34	1.46
Dermatan Sulfate Biosynthesis (Late Stages)	0.36	1.8
Hepatic Fibrosis / Hepatic Stellate Cell Activation	0.51	1.82
ErbB4 Signaling	0	1.84
NGF Signaling	0.65	1.91
Transcriptional Regulatory Network in Embryonic Stem Cells	0	2.02
Natural Killer Cell Signaling	0.41	2.12
Growth Hormone Signaling	0	2.95

B

H3K27me3 Dataset Roadmap Epigenomics Project	Length Dataset # peaks	Length Dataset # genes	Overlap with UC genes (p-value<0.0001)
Spleen	890810	882376	222
UCSD-H1 BMP4 Derived Trophoblast Cultured Cells	1325560	1313308	222
Mobilized CD34 Primary Cells	1153729	1143306	221
Gastric	792094	784187	221
Rectal Mucosa	648465	641873	220
Sigmoid Colon	767506	759234	220
Brain Germinal Matrix	362173	357451	218
Pancreas	749896	742464	218
Small Intestine	682839	675308	218
CD4+ CD25- CD45RA+ Naïve Primary Cells	505680	500918	217
CD4+ CD25int CD127+ Tmem Primary Cells	468281	463475	217
Brain Substantia Nigra	711099	704115	217
CD34 Primary Cells	962729	954526	216
H1	463280	457438	216
Aorta	793452	785640	214
Colonic Mucosa	265347	261769	213
Brain Dorsolateral Prefrontal Cortex	396941	392869	213
Adipose Nuclei	390468	386747	212
CD4 Naïve Primary Cells	474800	470272	212
CD8 Memory Primary Cells	302461	298671	209
Duodenum Smooth Muscle	318850	315499	208
K562 Leukemia Cells	326161	321774	208
CD8 Naive Primary Cells	492160	487211	204
Lung	452696	447986	204
Brain Anterior Caudate	343070	339092	203
Primary Mononuclear cells from peripheral blood	238012	235471	202
Brain Cingulate Gyrus	347751	344039	201
Brain Hippocampus Middle	318972	315716	201
Bone Marrow Derived Cultured Mesenchymal Stem Cells	278821	275678	197
Ovary	479447	474996	197
Primary Hematopoietic Stem Cells	472792	467751	192
CD4+ CD25- CD45RO+ Memory Primary Cells	239940	237228	186
Liver	389394	385107	179

C

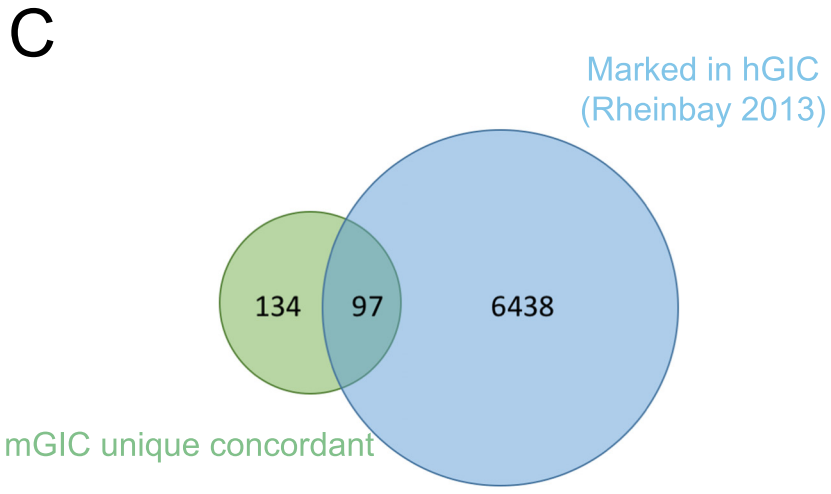

Ricci et al. Figure S2

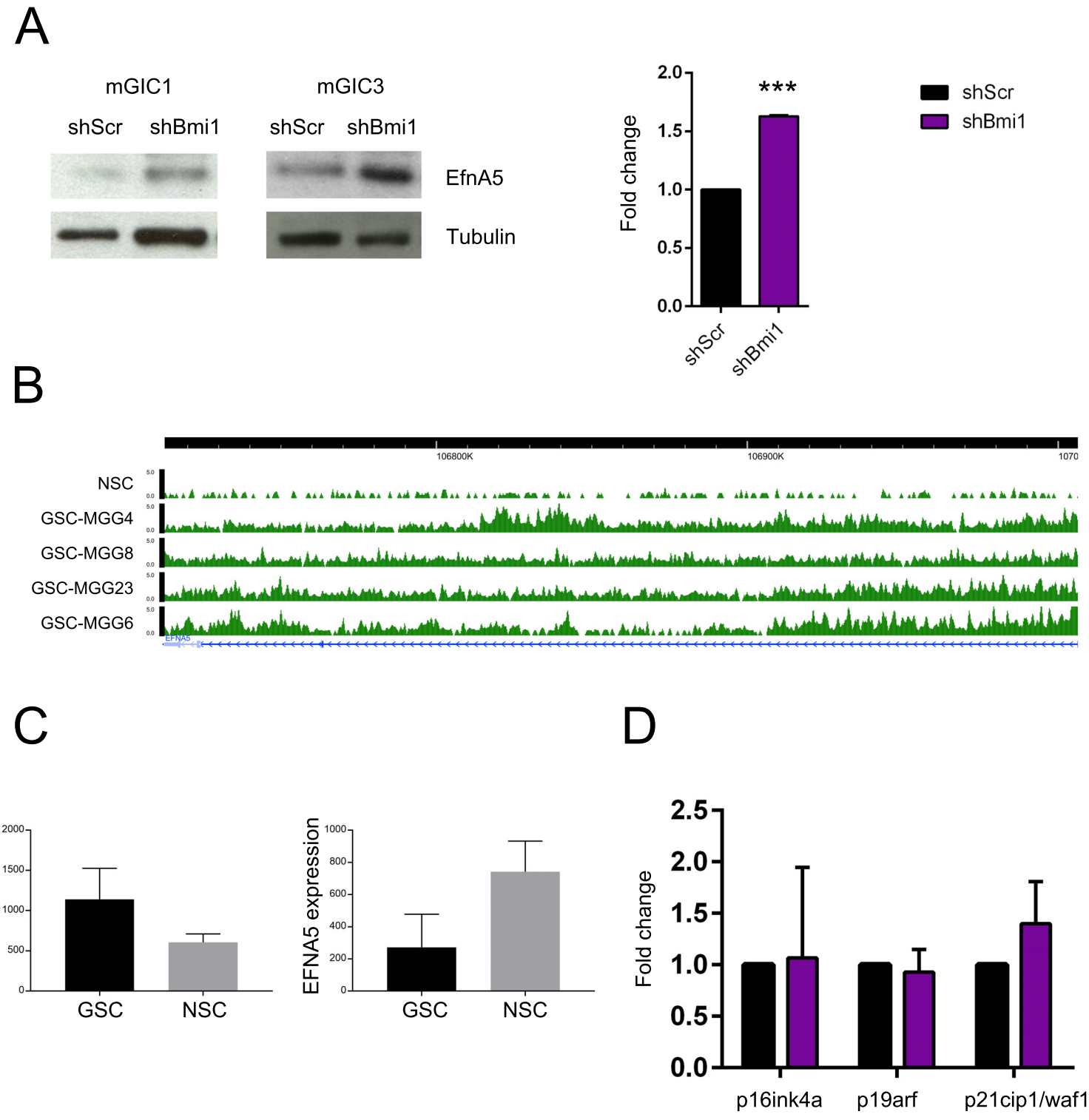

A

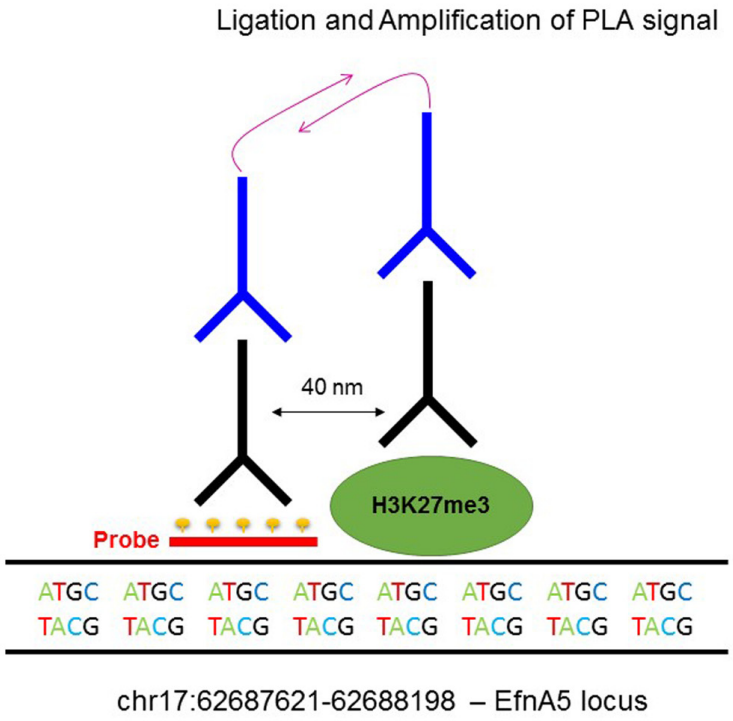
Ligation and Amplification of PLA signal
40 nm
H3K27me3
Probe
ATGC ATGC ATGC ATGC ATGC ATGC ATGC ATGC
TACG TACG TACG TACG TACG TACG TACG TACG
chr17:62687621-62688198 – EfnA5 locus

B

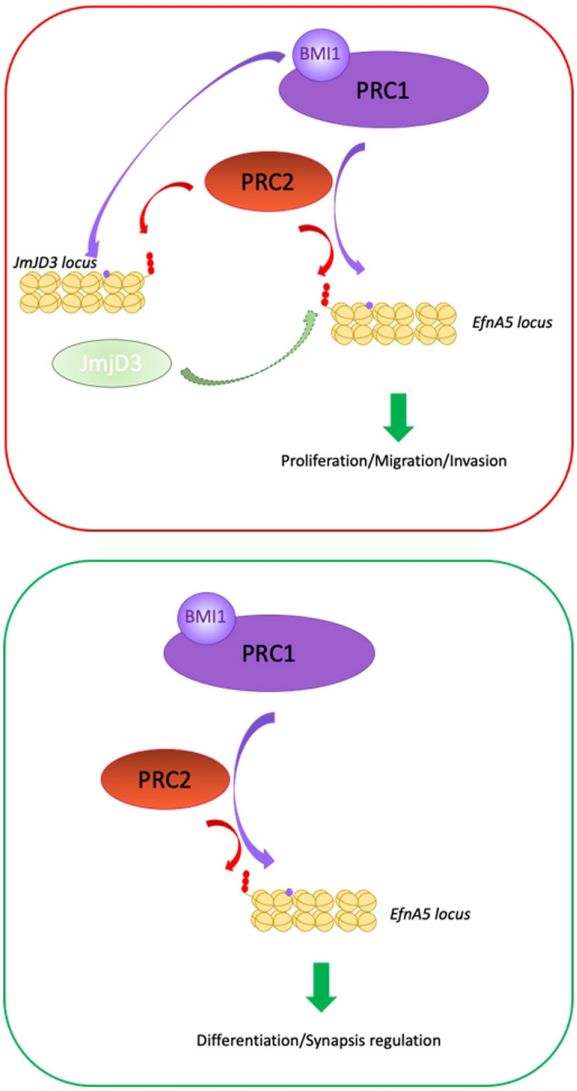
BMI1
PRC1
PRC2
JmJD3 locus
EfnA5 locus
JmjD3
Proliferation/Migration/Invasion
BMI1
PRC1
PRC2
EfnA5 locus
Differentiation/Synapsis regulation

Ricci et al. Figure S4

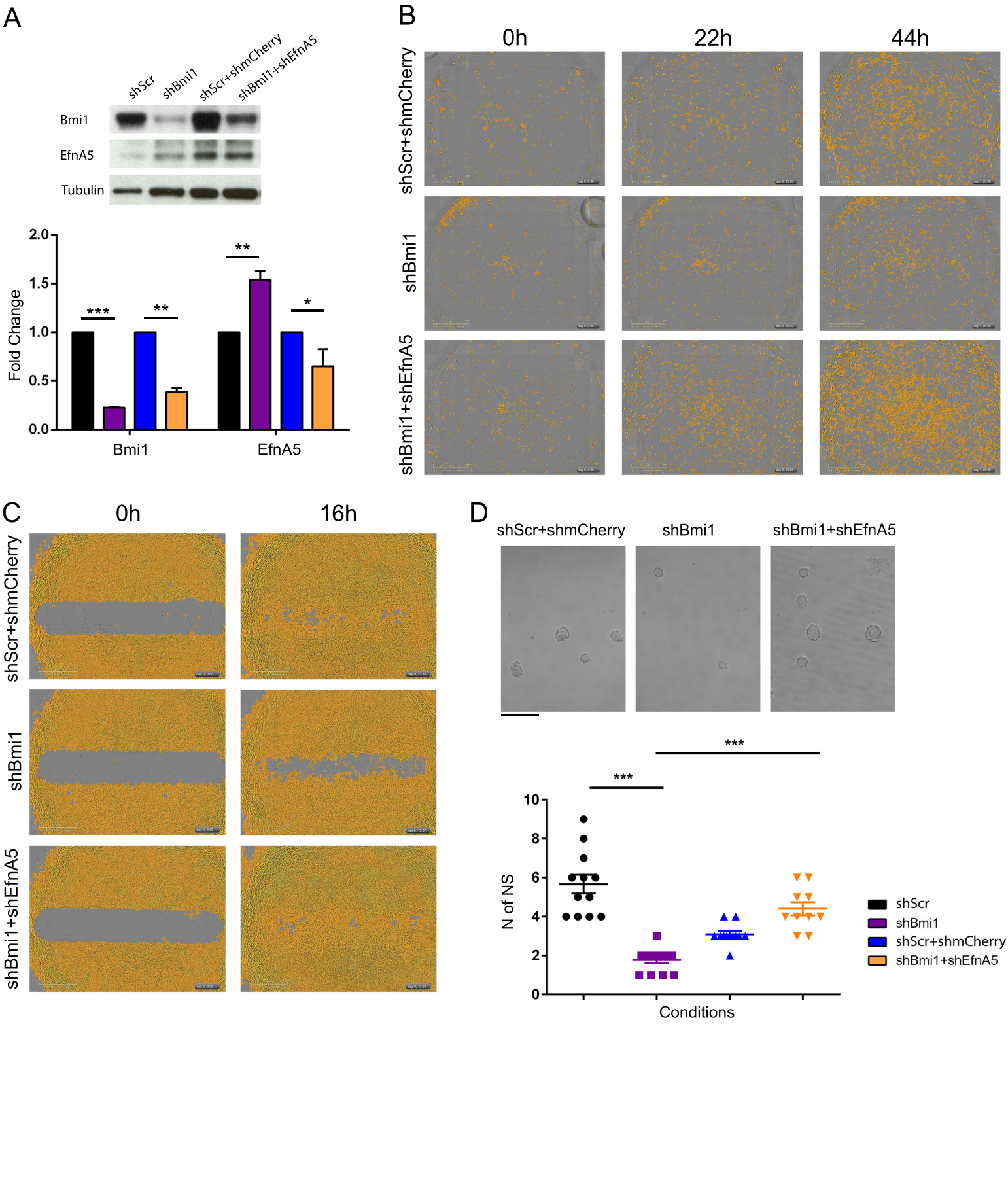

Ricci et al. Figure S5

A

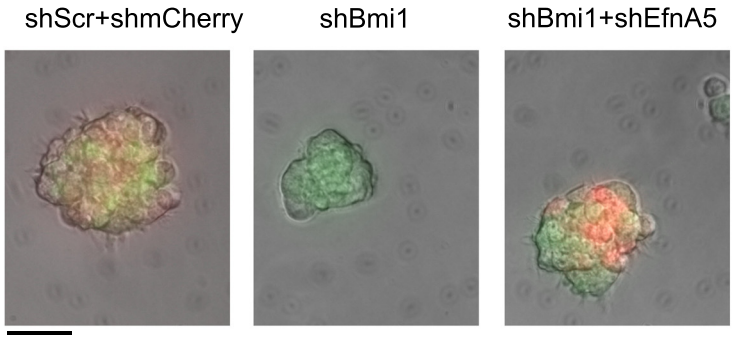

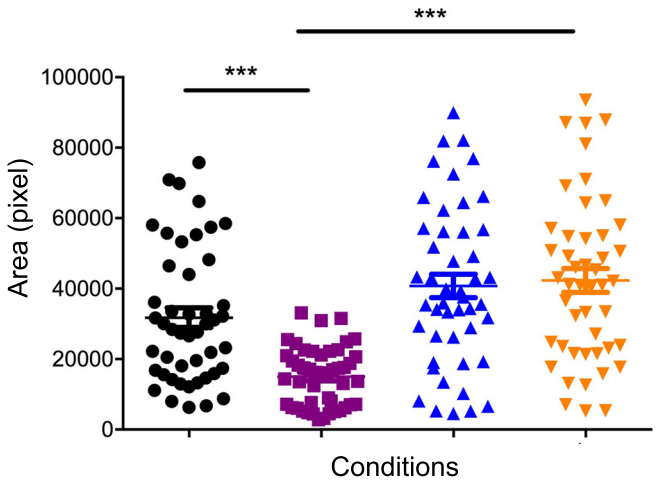

B

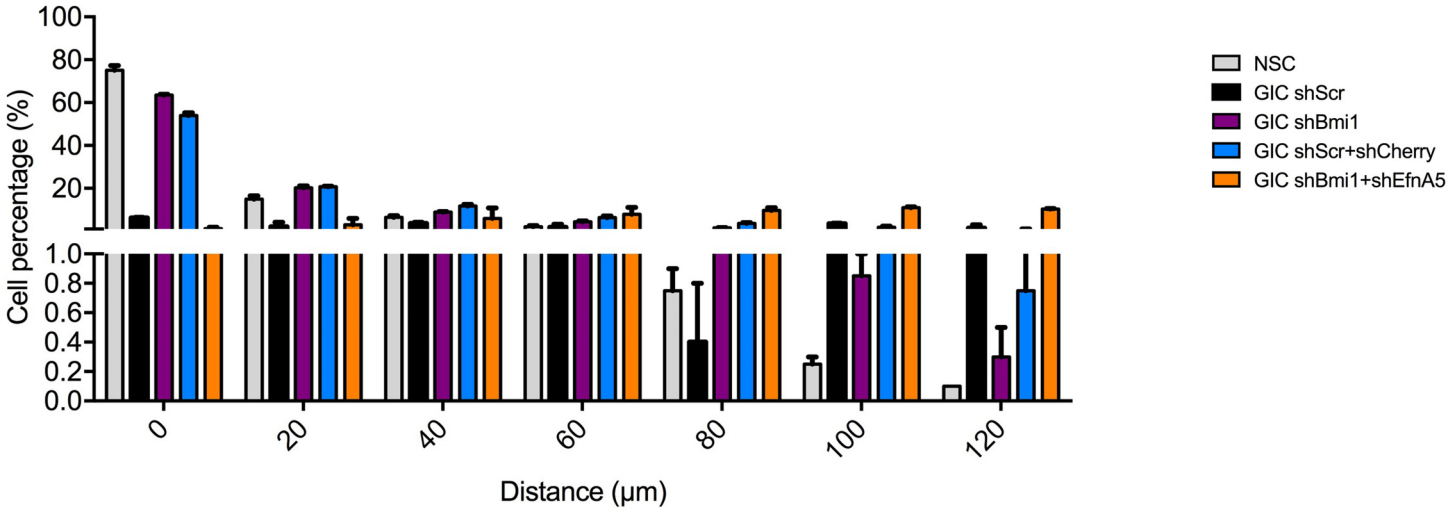

Ricci et al. Figure S6

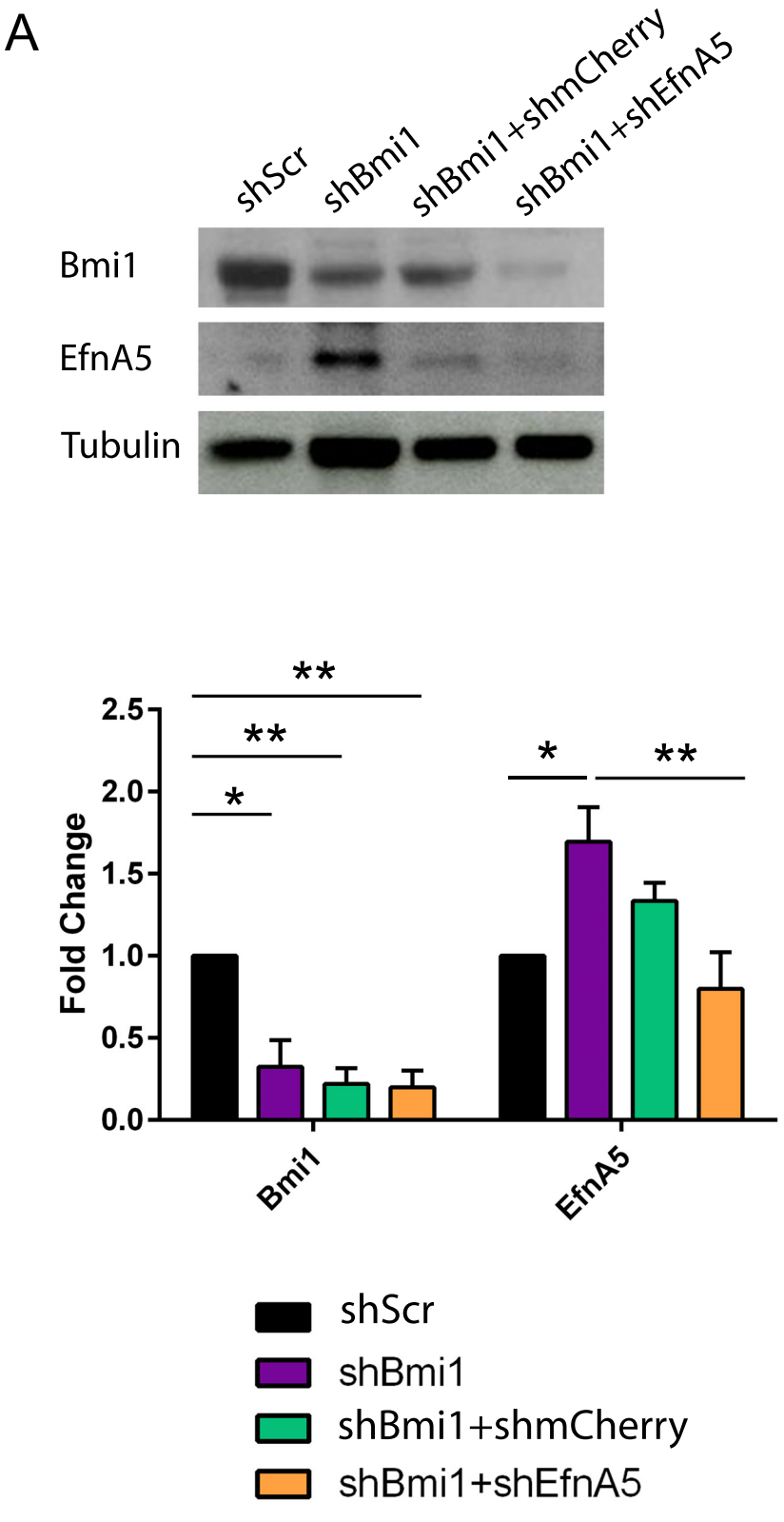

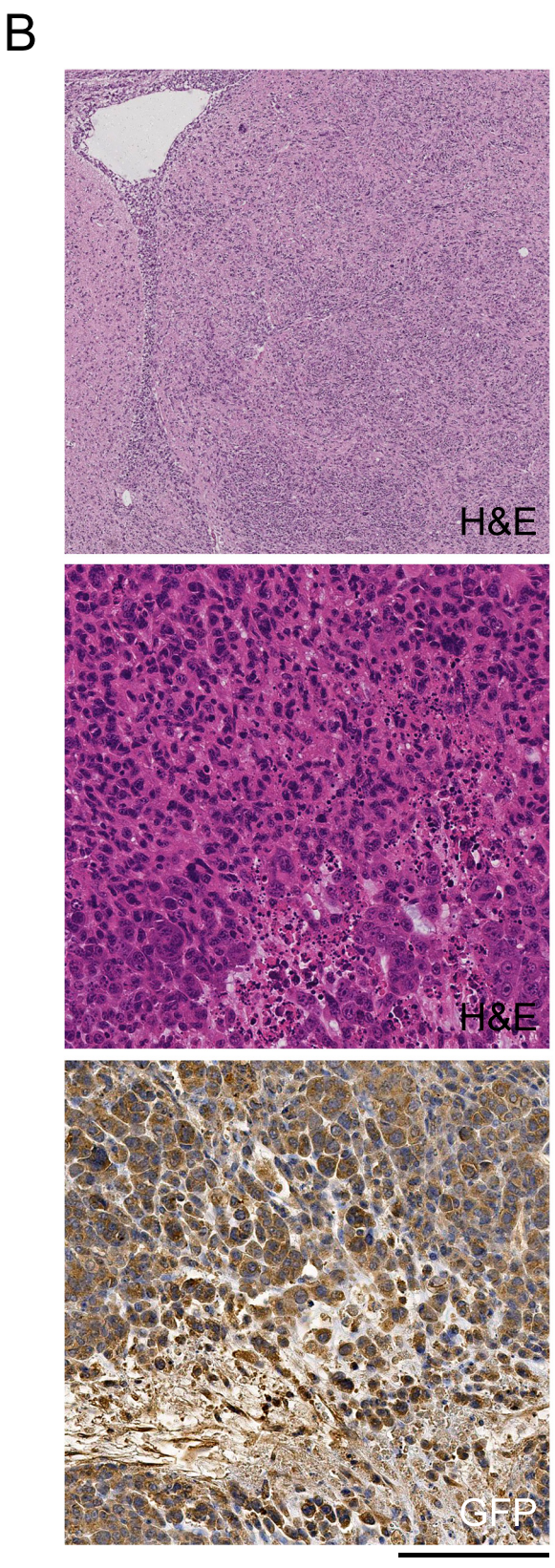

Ricci et al. Figure S7

A

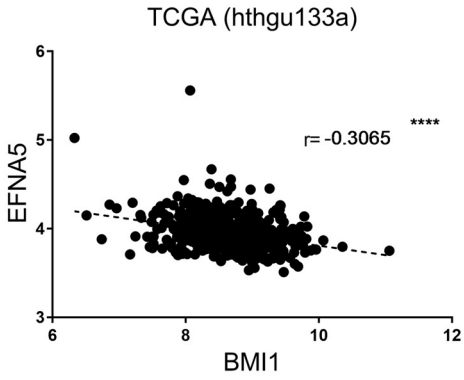

B

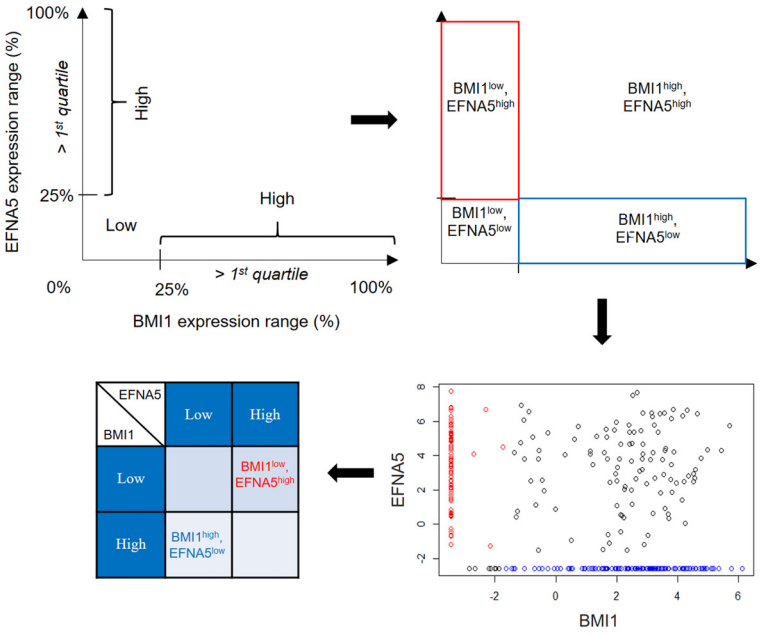

C

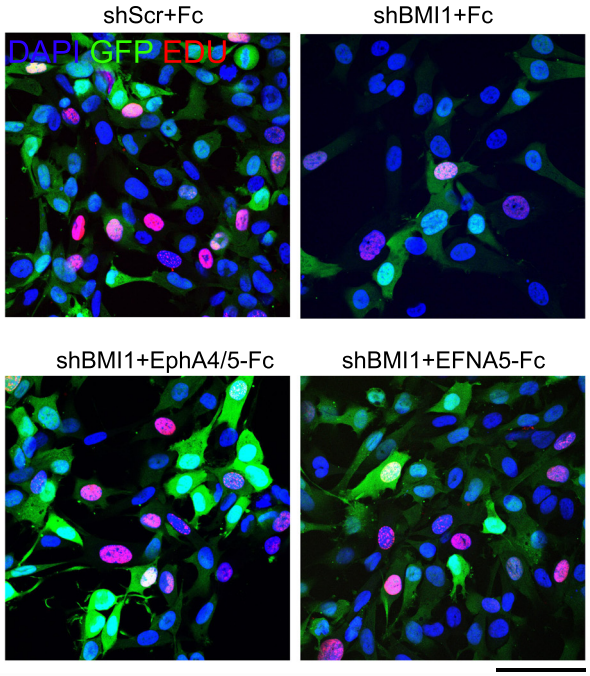

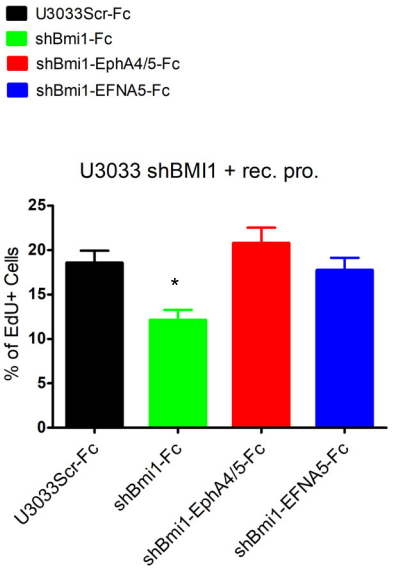

D

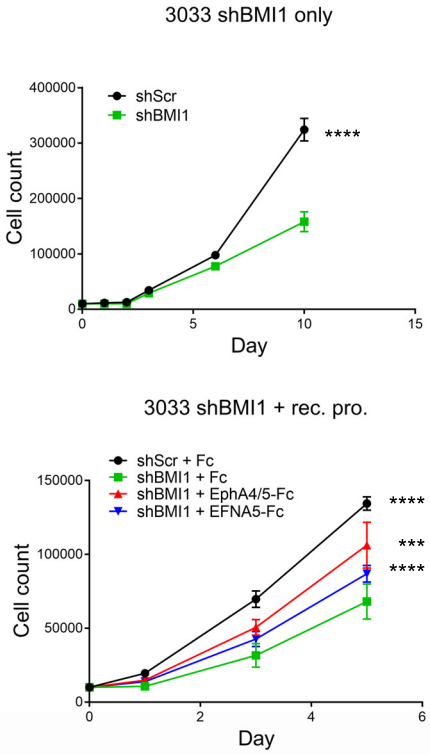

Ricci et al. Figure S8

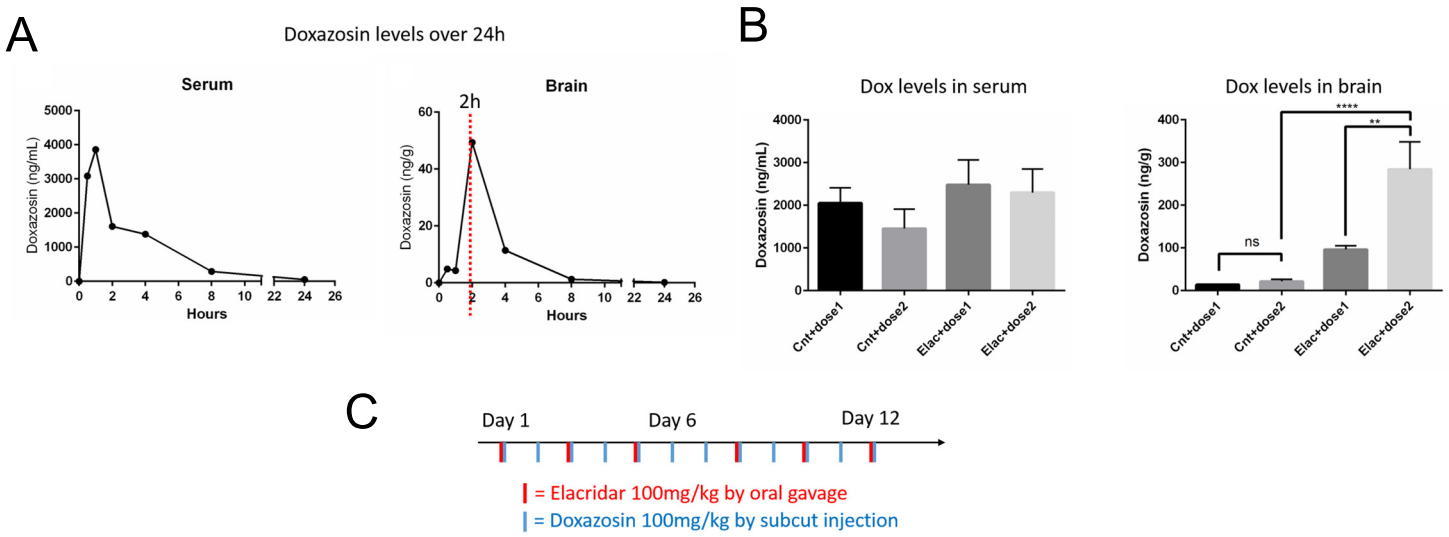

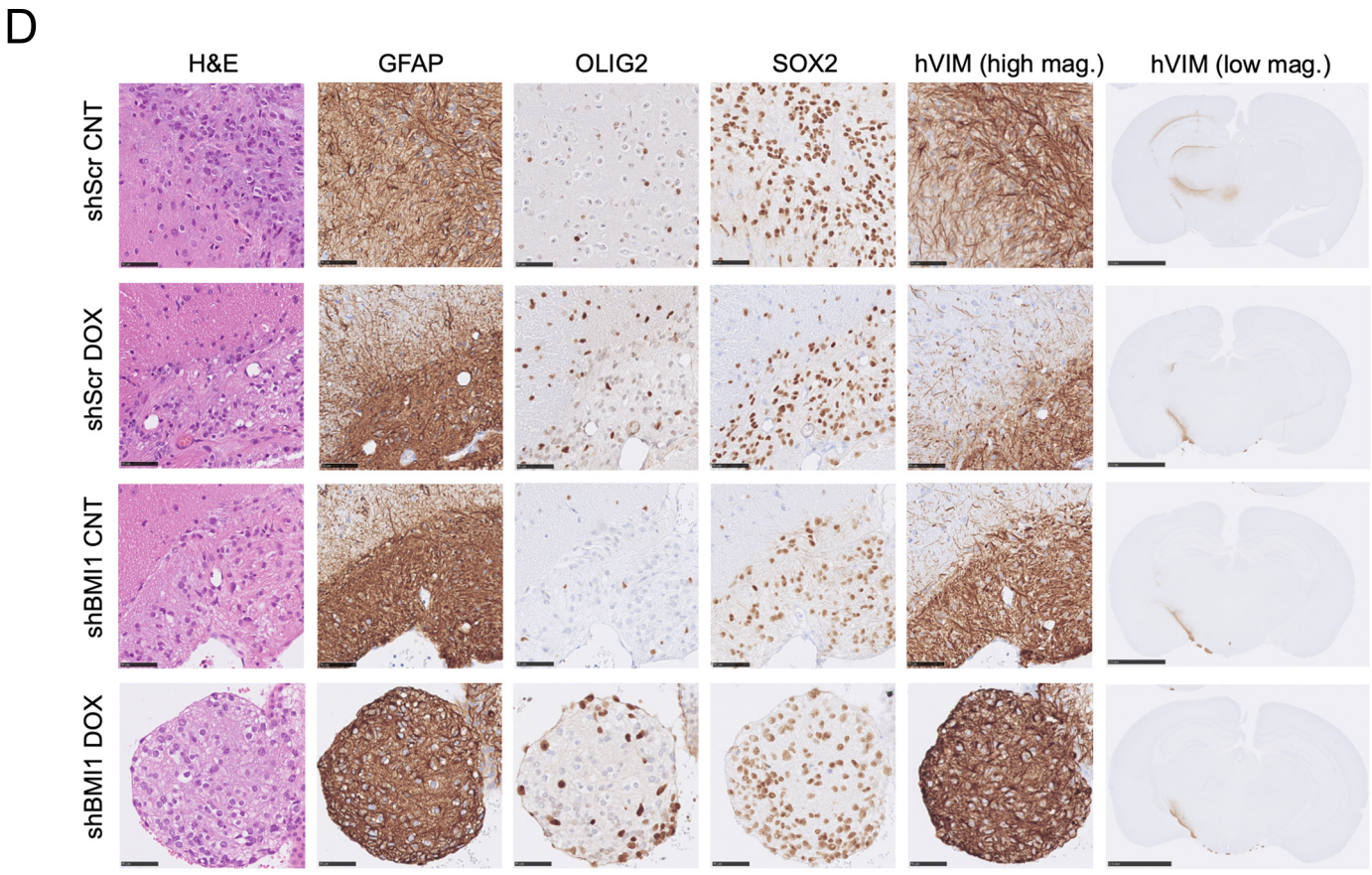

Materials and Methods

Generation of mice and genotyping

Transgenic *STOPFloxBmi1* mice were previously generated in our laboratory [11]. Activation of Bmi1 overexpression was obtained in embryos by crossing *STOPFloxBmi1* and *NestinCre* mice to generate double transgenic animals, as previously described [11].
All procedures were carried out according to the Home Office Guidelines (Animals Scientific Procedures Act 1986, PPL 70/6452 and P78B6C064). Ear notches of transgenic mice and tails of transgenic embryos were digested in lysis buffer (50 mM Tris pH 8.0, 100 mM NaCl, 100 mM EDTA and 1% SDS) and Proteinase K (Biolabs) at 55°C, 700 rpm overnight, or for three hours respectively. The DNA was subsequently precipitated in isopropanol (Fisher Scientific) and dissolved in pre-warmed PCR-grade water. Genotypes of mice were determined by PCR as described previously [11 7]. Standard agarose gel electrophoresis was used to visualise the band of interest.

Cultures

Primary NSC cultures were prepared from E16.5 *STOPFloxBmi1;NestinCre* transgenic and control wild type embryos. Cerebral hemispheres were collected by brain dissection and NSC from the SVZ were isolated using a Papain dissociation kit (PDS, Worthington) and cultured as neurospheres (NS) or as adherent monolayer (adh). Primary mouse NSC were plated at $4x10^4$ mL^{-1} density and grown as NS in culture medium composed of DMEM/F12 (Invitrogen), mouse recombinant EGF (20ng/ml, Peprotech,) and human recombinant b-FGF (20ng/ml, Peprotech, #AF-100-18B), 2% B27 (Invitrogen) and 1X Pen/Strep (Sigma Aldrich). Every 3-4 days the NS were mechanically dissociated and plated under the same conditions. For adh cultures, a single-cell suspension obtained from primary NS was plated at 10^5 cm^{-2} density. NS were plated on to a 90 µg/mL matrigel-coated (Corning) flask or dish in culture medium.

Primary mouse $PTEN^{F/F};P53^{F/F}$ NSC and mGIC were obtained from Sebastian Brandner, Institute of Neurology, University College of London, UK. Deletion of $PTEN^{F/F};P53^{F/F}$ cassette in NSC was achieved by *in vitro* AdenoCre infection as described previously [5]. Primary mGIC were cultured as NS or adh monolayer in the same culture medium used for NSC. For adh mGIC, flasks or dishes were first double-coated with 0.01 mg/mL poly-L-lysine (Sigma

Aldrich) in PBS for 30 minutes at room temperature, and then with 0.01 mg/mL Laminin (Sigma Aldrich) in PBS for 30 minutes at 37°C. Dissociation between passages was performed enzymatically with trypsin/EDTA (Invitrogen).

For EfnA5 pathway activation, mGIC were treated with 8µg/mL recombinant mouse EfnA5 Fc chimera (R&D Systems, #7396-EA) or IgG1 Isotype Control Clone 11711 (R&D Systems, #MAB002) pre-clustered with 4µg/mL anti-Fc (anti-mouse Alexa-546, ThermoFisher Scientific) in culture medium for 2 hours at 37°C. For prolonged assays the pre-clustered compound was refreshed every 24 hours.
To inhibit the activity of Ezh2, adh mGIC were plated at growth density with growth medium containing 5 µM Ezh2i (GSK-126, Chemietek) 24 hours prior to immunocytochemistry (ICC). Transient overexpression of JmjD3 was obtained by nucleofection (Amaxa, Lonza) of 10^6 adh mGIC with 5 µg of FlagJmjD3LeGO-iC or control LeGO-iC (Addgene). 24 hours later, cells were fixed for ICC. For viral transduction, adh mGIC were plated at growth density in culture conditions 24 hours beforehand. Transduction was performed by adding 8 MOI of AdenoCre particles or 20 MOI of lentiviral particles containing the plasmids shBmi1 (Dharmacon, Clone Id V2LHS_48576,), shEfnA5-32 (GeneCopoeia) or shEfnA5-34 (GeneCopoeia) overnight. shScramble and shmCherry plasmids, both containing a scramble sequence, were used as controls. Growth medium was then changed and the cells were allowed to recover before further assays were performed.

hGIC were obtained from HGCC (http://www.hgcc.se); they were cultured as adherent cells in Neurobasal and DMEM/F12 media (1:1 mix) containing N2 and B27 supplements (Invitrogen) and human recombinant FGF and EGF (10 ng/ml, PEPROTECH). Primaria dishes (BD Biosciences) coated with mouse laminin (Sigma-Aldrich) were used to allow adherent growth as described previously (Pollard et al., 2009). For EFNA5 pathway blockade, hGIC were treated with 4µg/mL recombinant human EFNA5 Fc chimera (R&D Systems, #374-EA-200), or EPHA4 Fc chimera (R&D Systems, #6827-A4-050) and EPHA5 FC chimera (R&D Systems, #541-A5-200), or IgG1 Isotype Control (R&D Systems, #110-HG-100), replaced daily in fresh media. For doxazosin treatment, cells were treated every other day with the stated concentration of doxazosin (Abcam, ab120754) in DMSO, with a final volume of 0.2% of complete medium. 0.2% DMSO was used as the vehicle control.

Cell lines used in this study are primary lines either derived from mouse brains or human tumours, they have been characterised by transcriptomic profiling and cultured according to best practice, including contamination-screening.

ChIPSeq and RNASeq

The chromatin immunoprecipitation (ChIP) assay was performed on two biological replicas of control NSC, two biological replicas of NSC Bmi1^{Over} (isolated from *NestinCre;STOPFloxBmi1*) and two mGIC [5] according to previously published protocols with minor modifications [2]. Chromatin was sonicated to get fragments of 100 to 500 bp and immunoprecipitated with 10 µL of anti-H3K27me3 (Active Motif, #39155). ChIPSeq libraries were prepared following the Illumina protocol and ligated to standard PE adaptors and sequenced on a HiSeq2000. For RNASeq, 200 ng of total RNA was used to prepare RNASeq libraries using the TruSeq RNA kit from Illumina following the instructions provided in the supplier's manual, and sequenced on HiSeq2000. ChIPSeq and RNASeq data are available in the array express database (http://www.ebi.ac.uk/arrayexpress/), accession numbers will be available at time of publication.

RNASeq: Adaptor sequence and other artefacts were removed from sequence reads using the Trimgalore tool (www.bioinformatics.babraham.ac.uk/projects/trim_galore/). After trimming and quality control, reads were aligned to the mm10 mouse genome using STAR [3]. Further quality and biotype filtering was performed in R with NOISeq Bioconductor package [10]. Trimmed mean of M-values (TMM) normalization was applied to the dataset and differential expression (DE) analysis was performed using the Bioconductor package edgeR in R [9], with a Quasi-Likelihood F-test (QLF) and an FDR cut-off of 0.05.

ChIPSeq: Adaptor sequence and other artefacts were removed from sequence reads using the Trimgalore tool. After trimming and quality control, reads were aligned to the mm10 mouse genome using Bowtie v2.3.4 (sourceforge.net/projects/bowtie-bio/files/bowtie2/), allowing up to one mismatch per read and discarding multi-mapped reads. Read totals after trimming and alignment varied between 14.8M and 3.5M in mGIC replicates, 6.4M and 4.5M in NSC Bmi1^{Over}, 17.4M and 3.9M in NSC replicates.

After performing post-alignment quality checks, based on the number of final reads, quality scores and the analysis of fingerprint plots (not shown), we decided to discard the weakest samples and perform further ChIPSeq analysis only on one replicate per condition.

The MACS2 algorithm [14] was used to call H3K27me3 peaks (subroutine *callpeak*) and perform the differential binding (DB) analysis (subroutine *bdgdiff*). The shifting model and the dynamic lambda were both disabled (as they are not recommended for histone modification analysis), the "broad mark" option was enabled and a minimum fold enrichment of 2 was selected with an FDR (--broad-cut-off) of 0.05. Finally, a minimum length of differential regions of 250 bp and a maximum gap (to merge nearby regions) of 200 bp were considered, in concomitance with a log likelihood ratio cut-off of 2 to call differential regions between conditions.

The Bioconductor package GenomicRanges [6] was used to find overlaps of peak genomic coo rdinates between different conditions, i.e. mGIC vs NSC, or mGIC vs NSC Bmi1^{Over}, whereas C hIPSeeker [12] was used for the peak annotation and the promoter characterisation within 5 K b.

RNASeq/ChIPSeq combined analysis: Because we would expect to see reduced expression of a gene harbouring an H3K27me3 peak in a promoter proximal region, we identified peaks in NSC, NSCBmi1^{Over} and mGIC datasets that showed significantly reduced gene expression at the locus containing an H3K27me3 peak and defined these peaks "expression concordant". To characterize orthologous genes between murine and human datasets, biomaRt package in R was used [4].

Hierarchical Clustering and Heatmaps: Clustering and heatmap generation for gene expression data and H3K27me3 peaks were performed using various packages in R such as gplots and RColorBrewer (https://cran.r-project.org/) and the Python suite deepTools v. 3.1.3 [8].

Pathway analysis: We used Ingenuity Pathway Analysis (Qiagen, https://www.qiagenbioinformatics.com/products/ingenuity-pathway-analysis/) to analyse pathways and networks that showed significant enrichment in the various gene sets generated by our analysis. The enrichment for each term was tested using hypergeometric

distribution and p-values were corrected using an FDR procedure. All terms with a FDR <0.05 were considered enriched.

RMA log2 transformed signal intensity values were downloaded from the HGCC database website (hgcc.se). Pearson correlation coefficients and relative p-values were calculated using GraphPad Prism 7.

A schematic for the generation of the contingency tables in Fig.7A is shown in Fig.S7B. Ranges of expression for both BMI1 and EFNA5 were determined, separately for each single-cell RNASeq dataset analysed. The first quartile was chosen as the cut-off to define the "low expression" and "high expression" segments. Analysis with other cut-off values such as 15% and 50% (median) was also performed and the outcome did not show a significant difference (data not shown). Four regions of expression, each with a different BMI1/EFNA5 profile, can be obtained by combining the "low" and "high" segments for both genes. A contingency table with the counts for all regions was created for each dataset and both Fisher's and Barnard's exact tests were applied, to determine whether the distribution of counts among the aforementioned regions was non-random.

R v. 3.5.1 was used to run all aforementioned packages whereas Python v. 2.7.15 was used for MACS2 and deepTools routines.

Western Blot

Protein homogenates were obtained using RIPA buffer containing protease cocktail inhibitors (Santa Cruz Biotechnology). Protein concentration was determined by BCA assay (Pierce) and an equal amount (10-60µg) was loaded into a NuPAGE Novex 3-8% Tris-Acetate or a 4-12% Bis-Tris protein gel (ThermoFisher Scientific). Proteins were separated by SDS-PAGE and blotted onto a nitrocellulose membrane (Whatman). Membranes were blocked with 5% non-fat dried milk (Santa Cruz)-0.1% TWEEN-PBS and incubated with the primary antibody diluted in blocking solution according to each antibody's recommendation: anti-Bmi1 (1:1000, mouse monoclonal Millipore, Clone F6, 05-637), anti-H3K27me3 (1:5000, rabbit polyclonal Millipore, 07-449), anti-EFNA5 (1:400, mouse monoclonal NOVUS Biologicals, Clone 1F12, H00001946-M01), anti-Tubulin (1:10000, mouse monoclonal Sigma Aldrich, T6199), anti-GAPDH (1:1000, mouse monoclonal Sigma, Clone 71.1, g8795), anti-H3 (1:50000 rabbit polyclonal Millipore, 07-690), anti-EphA2/A3/A4 (1:500, Abcam, ab196899), anti-Phospho-EphA2/A3/A4 (1:500, Abcam, ab62256), anti-ERK1/2 (1:1000, Cell Signalling

Technology, 4695), anti-Phospho-ERK1/2 (thr202/Tyr204) (1:1000, Cell Signalling Technology, 4370). Membranes were then incubated with the peroxidase-conjugated mouse secondary antibody 1:5000 or rabbit secondary antibody 1:10000 (GE Healthcare, NA931V and NA934V respectively) and visualised on a film using ECL kit (GE Healthcare). Quantification of protein expression was performed by densitometric analysis and normalised with ImageJ software.

Immunocytochemistry

Adh mGIC were plated as a monolayer on coated coverslips. After fixation with 4% PFA (Sigma Aldrich) and permeabilisation with 0.1% TritonX-PBS (Sigma Aldrich), cells were blocked with 10% NDS (normal donkey serum, Millipore) / PBS and incubated overnight at 4°C with the primary antibodies: phalloidin (Phall-488 1:400, ThemoFisher Scientific, A12379), GFAP (1:500, rabbit polyclonal Dako Denmark, Z0334), Nestin (1:500, mouse monoclonal, Chemicon, MAB353). Coverslips were mounted with Vectashield mounting medium with DAPI (Vector Laboratories). The staining was developed using Alexa fluorescent conjugated secondary antibodies (ThemoFisher Scientific) and images were acquired using a Leica DM5000 Dual Camera Epifluoresence microscope. For phalloidin intensity measurements, the outline of positive cells was manually traced for ten randomly selected areas for each condition, and then staining intensity (integrated density) was measured for each cell with ImageJ software. Background was subtracted and resulting values were normalised against the control condition and expressed as a fold change. Statistical analysis (one-way ANOVA) was performed with GraphPad software. For cellular process length measurements, 10 random high power fields were captured for each condition and all cell processes (yellow arrowheads in Fig. 4A highlight example processes) were measured manually with ImageJ for each field. Measurements were taken in pixels then converted to µm using magnification properties of objectives used. Length values were then averaged for each condition, and are expressed as a fold change of the control condition. Statistical analysis (one-way ANOVA) was performed with GraphPad software. For hGIC, shScramble or shBMI1 transduced cells were plated at growth density. After five days of daily treatment with 4ug/ml of recombinant mouse proteins (see above for details) cells were then fixed, blocked in 10% normal donkey serum (NSD, Millipore) and Tween20 (0.1%) in PBS. Primary antibody incubation with anti-Eph receptor A2/3/4 (Abcam, ab62256,

1:500) for 3 hours was followed by 1 hour incubation with AlexaFluor-546 (ThermoFisher). Coverslips were mounted with Vectashield mounting medium with DAPI (Vector Laboratories). Images were acquired using a Zeiss 710 confocal microscope and pictures were analysed with ImageJ software. Investigators were blinded to the group allocation during the analysis.

EdU staining

The Click-iT® EdU Alexa Fluor® 594 Imaging Kit (ThermoFisher) was used to assess EdU incorporation following manufacturer's instruction. Briefly, transduced hGIC were seeded on polylysine-coated coverslips in triplicates. The following day, cells began daily treatment with recombinant proteins (see above for details) for five days. On the fifth day, cells were treated with 10μM of EdU for three hours before being fixed in 4% paraformaldehyde (PFA), washed, blocked and incubated with Click-iT® reaction cocktails containing Alexa Fluor® azide. Five representative images (40X magnification) of each sample were captured using a Zeiss 710 Confocal Microscope. The percentage of positive nuclei was calculated as the ratio between EdU-positive cells and the total number of nuclei counted using ImageJ software.

Cloning

To overexpress JmjD3 in our cultures, the cassette FlagJmjD3 from the plasmid pCDNA-FlagJmjD3 (gift of Giuseppe Testa, IEO, Italy) was cloned into the lentiviral plasmid LeGO-iC (Addgene, #27362) for the production of lentiviral transducing particles (see below). Both plasmids were digested with BamHI-HF and NotI-HF restriction enzymes (New England Biolabs). The insert (FlagJmjD3) and the backbone were ligated at a 1:3 molar ratio with the T4 ligase enzyme (New England Biolabs) overnight at 16°C. Afterwards, TOP-10 bacteria one shot chemical competent cells (Invitrogen) were transformed with the ligation mixture according to the manufacturer's instructions. Successful ligation was tested by BamHI-HF and NotI-HF restriction digestion of plasmid DNA (FlagJmjD3LeGO-iC) extracted from positive colonies and mutations were excluded by Sanger sequencing with four pairs of primers (F1 5'-CCTATTGACTGAGTCGCCCGGATC-3', F2 5'-CAGCAGTAGCAGTAACAACAC-3', F3 5'-AGTCCTGCATCAGGTGCTAC-3', F4 5'-GCTAAATACGCACAGTACCAGG-3', R1 5'-AATGGTCAGCGCCAGGAATG-3', R2 5'-AGATGACGAGGAAACCGAGG-3', R3 5'-TCACTCTCCCTCTCCTCCTG-3', R4 5'-GAAGCCGCTTGGAATAAGGC-3'). Results were aligned to

the mouse JmjD3 (KDM6B) sequence (genome assembly GRCm37) available on the NCBI BLAST website (http://blast.ncbi.nlm.nih.gov/Blast.cgi).

Lentiviral production

Second generation lentiviral particles were produced to deliver the following plasmids: FlagJmjD3LeGO-iC, shScramble, shBmi1, shmCherry, shEfnA5-32, shEfnA5-34, and Luciferase. 4-5x10^5/cm^2 HEK 293T cells were transfected with the lentiviral plasmids pCMV-G, pCMV-HIV1 and the plasmid of interest. After 48 hours in culture, the supernatant was collected, cell debris were removed by filtration (0.45 PVDF filter, Sartorius) and the lentiviral particles were precipitated with polyethylene glycol (Sigma Aldrich) and stored at at 4°C for 16 hours-4 days. Lentiviral particles were concentrated by centrifugation (30 minutes, 1500xg, 4°C), resuspended in sterile PBS and stored at -80°C.

Transducing units were then determined by plating 0.5 x10^5 HEK 293T cells into 12-well-dishes and exposing them to serial dilutions, 10^{-1} to 10^{-5}, of the lentiviral supernatant. Cells were collected 96 hours from the transduction and the percentage of GFP- or mCherry-positive cells was determined by FACS (BD FACS Canto II or Aria III Cell Sorter). The titre in transducing units per ml (TU/ml) was calculated according to the following formula: ((% positive cells/100) x no. transduced cells)/volume of virus (mL).

RNA extraction, RT and qPCR

For mGIC, 5x10^5-10^6 cells were harvested and RNA extraction was performed using Micro or Mini RNeasy kit (Qiagen). RNA was then treated with DNaseI (Invitrogen) and 1µg was retrotranscribed with SuperScriptIII (Invitrogen). 10-20ng of cDNA template and FAM labelled probes were used to perform Taqman assay (Invitrogen). Each reaction was performed in triplicate and normalisation was carried out against the housekeeping gene Gapdh. The following Taqman probes were used for gene expression analysis: **Gapdh** (Mm99999915_g1), **Bmi1** (Mm03053308_g1), **EfnA5** (Mm01237700_m1), **Jph3** (Mm00517489_m1), **Lrfn2** (Mm01281423_m1), **Scrt1** (Mm00459966_m1), **Cpne2** (Mm00467840_m1), **EphA2** (Mm00438726_m1), **Wnt7a** (Mm00437356_m1), **Cacna1g** (Mm00486572_m1), **Grin2a** (Mm00433802_m1), **Cacna1h** (Mm00445382_m1), **Cacna1a** (Mm00432190_m1), **Eya2** (Mm00802562_m1) **Cabp1** (Mm00600215_m1).

Chromatin Immunoprecipitation followed by qPCR (qChIP)

ChIP experiments were performed on mGIC cultured as NS. 5×10^6 cells were dissociated into a single-cell suspension and resuspended in 10 mL of sterile PBS. Cells were cross-linked in 1% formaldehyde (Sigma Aldrich) for 15 minutes rocking at room temperature. Reaction was quenched with 0.125 M glycine (Santa Cruz Biotechnology) for 5 minutes rocking at room temperature. The mixture was centrifuged for 5 minutes at 4°C, 2000 rpm and the pellet was washed twice with cold sterile PBS to remove any formaldehyde residue. The cell pellet was then incubated with Washing Buffer (10mM HEPES/KOH pH 7.9, 85mM KCl, 1mM EDTA, 0.5% IGEPAL, protease inhibitor cocktail) for 30 min on ice. After 5 minutes centrifugation at 4°C, 4000 rpm, the pellet containing the nuclei was incubated in Lysis Buffer (1 mM PMSF, 50 mM Tris/HCl pH 7.4, 1% SDS, 0.5% Empigen BB, 10 mM EDTA, 1X protease inhibitor cocktail Roche) on ice for 30 minutes. Chromatin was then transferred into a Bioruptor Pico Microtube (Diagenode) and sonicated with a Bioruptor machine (Diagenode) for 7 cycles, 30 seconds ON/ 30 seconds OFF to achieve an average fragment size of 100 – 1,000 base pairs (bp). Beads (Invitrogen) were blocked with 2.5 mg/mL BSA (Sigma Aldrich) and 1 mg/mL salmon sperm (Sigma Aldrich) for 2 hours rocking at 4°C**.** Afterwards, the chromatin was precleared for 2 hours at 4°C with 1 mg of blocked beads (Invitrogen). 15-20 µg of precleared chromatin were immunoprecipitated with 2.5 µg of rabbit polyclonal H3 (Abcam, #A3912) or rabbit polyclonal H3K27me3 (Millipore, #07-449) antibodies overnight rocking at 4°C. The immunocomplexes were then incubated for 3-5 hours with rocking at 4°C and with 1 mg of beads previously blocked. Bead-immunocomplexes were washed for 5 minutes, rocking at 4°C with the following buffers: Washing Buffer A (50 mM Tris pH8.0, 150 mM NaCl, 1 mM EDTA, 0.1% SDS, 1% IGEPAL, 0.5% deoxycholate, protease inhibitor cocktail), Washing Buffer B (50 mM Tris pH8.0, 500 mM NaCl, 1 mM EDTA, 0.1% SDS, 1% IGEPAL, 0.5% deoxycholate, protease inhibitor cocktail), Washer Buffer C (50 mM Tris pH8.0, 250 mM LiCl, 1 mM EDTA, 1% IGEPAL, 0.5% deoxycholate, protease inhibitor cocktail). Immunocomplexes were eluted from the beads with an incubation for 40 minutes at 65°C, 1400 rpm with Elution Buffer (1% SDS, 0.1 M $NaHCO_3$) Proteins were reverse-crosslinked for 15 minutes at 37°C 650 rpm with RNaseA and degraded with Proteinase K overnight at 65°C, 650 rpm. DNA was extracted with standard phenol:chloroform:isamyl alcohol (25:24:1) precipitation and air dried. 2 µL of resuspended DNA was used to perform SYBR Green qPCR (Applied Biosystems) and determine the abundance of specific sequences within the immunocomplexes. Primers used

for the EfnA5 locus: **PS3.2 Fwd** 5'-AAAGATTGCTTTTCCTTCTGAG-3', **PS3.2 Rev** 5'-CTATCCTAGGCTAAGACACTGT-3', **PS3.5 Fwd** 5'-ATTGCACAAGAATACTCCTTAT-3', **PS3.5 Rev** 5'-TGACTCACTTGTACGGGAACAA-3'. H3-immunoprecipitated chromatin was used as reference for normalisation and enrichments were calculated using the ChIP-qPCR Data Analysis ΔΔCt method. Data are shown as fold changes of the percentage of INPUT and results of at least two independent biological replicates.

Proximity Ligation Assay, including probe generation and biotinylation

We cloned a 578 bp region spanning chr17:62687621-62688198 for EfnA5 locus into a TOPO TA Cloning vector (Thermo Fisher Scientific, 450641) according to manufacturer's instructions. FW: ACTGGTGGGACTCTCTCAAATTT and REV: AATGACTCACTTGTACGGGAACAA were used to clone the EfnA5 locus. NEB 5-alpha Competent E. coli cells (New England Biolabs, C2987H) were used for bacterial transformation and extraction of vector DNA. 1µg of plasmid DNA was then used as template to generate a biotintylated probe using Nick Translation Kit (Roche, 10976776001) and Biotin-14-dATP (Thermo Fisher Scientific, 19524-016). Plasmid DNA was incubated with nick translation reaction mix for 2 hours at 16 °C and stored at - 20 °C after the addition of 25 µM EDTA pH 8.0.

Cells were seeded on glass coverslips at a density of $10^5/cm^2$. Cells were then incubated in PBS 1X / Fish Skin Gelatin (FSG, Sigma G7765) supplemented with normal donkey serum at 10% and Triton-X at 0.1% for 1h RT in a humidity chamber. Slides were then dehydrated with washes of increasing ethanol percentages, 50%, 70%, 90% and 100% at RT, 10 min each. Dehydration was followed by an incubation in 1mM EDTA pH 8.0 at 40-45 °C for 20 min. Slides were incubated at 37 °C for 15 min. in 4-4.5 pH pepsin solution prepared as following: 100 mg of Pepsin (Sigma P7000), 5 mL of 1M TrisHCL pH 8.0, 2 mL of 200mM CaCl2, 2 mL of 0.5 M EDTA pH 8.0, 200µl of 5 M NaCl in a final volume of 100 mL of distilled water. Cells were then washed in PBS 1X for 5 min.

The probe was prepared in a final volume of 20 µL/slide using 2% of biotinylated probe, 1% mouse Cot-1 DNA (Thermo Fisher Scientific, 18440-016) and 70% of Hybridization Buffer: 500 µL of Formamide , 100 µL of Dextran Sulfate 50%, 100 µL of SSC 20X and 300 µL of distilled water. Probe mixture was denatured at 80 °C for 10 min. and immediately transferred to slides. Slides and probe mixture were heated once again at 80 °C for 10 min to encourage probe annealing, and then incubated overnight at 37 °C in a humidity

chamber. Following overnight incubation, slides were washed 3 times in SSC 2X and 0.1% NP-40 for 15 min. and then in PBS 1X for 5 min. At this point Duolink® In Situ Far Red Kit Goat/Rabbit (Sigma, DUO92013, DUO92003, DUO92005) was used. Slides were blocked using the provided solution at RT for 45 min. and then incubated at 4 °C overnight with polyclonal rabbit anti-H3K27me3 (Millipore, 07-449) diluted 1:200 and goat anti-biotin (Vector Laboratories, SP3000) 1:200 in antibody dilution solution. The next day cells were washed 3 times in wash buffer A for 5 min. and then incubated with PLA probes PLUS and MINUS diluted 1:5 in antibody dilution solution at 37 °C for 1 hour in humidity chamber. After 3 washes in wash buffer A for 5 min. ligation was performed using ligase diluted 1:40 in ligation stock 1:5 in water at 37°C for 30 min. in humidity chamber. Slides were washed 3 times in wash buffer A for 5 min. Amplification was performed using polymerase diluted 1:80 in amplification stock 1:5 in water at 37°C for 100 min in humidity chamber. Slides were washed 3 times in wash buffer B for 10 min and then wash buffer 0.01X for 5 min. Anti-mCherry antibody (Abcam, clone 1C51, ab125096) was diluted in 0.1% BSA , 1% normal donkey serum and PBS 1X 1:250 and incubated overnight at 4°C to detect transfected cells. Slides were mounted using Vectashield mounting medium with DAPI (Vector Laboratories).

In Vitro **Functional Assays**

Proliferation Assay

$1x10^3$ cells of adh mGIC were seeded in each well of a 96-well plate. Using an IncuCyte ZOOM Live-Cell Analysis System (EssenBioScience), wells were scanned and imaged every 2 hours for 2 days at 4X magnification. After background and cell debris subtraction, proliferation rate was assessed with the IncuCyte ZOOM Software (EssenBioScience) as occupied area (% confluence). At least two biological replicas with three technical replicates each are shown for every experiment.

$1x10^4$ cells of hGIC were seeded in each well of a 24-well plate. Cell counting was performed with Tryptan blue staining using a haemocytometer. At least two biological replicas with three technical replicates each are shown for every experiment.

Wound Healing Scratch Assay

$5x10^4$ cells of adh mGIC were seeded per well in a 96-well plate. A scratch was then made with a WoundMaker™ 96-pin tool (EssenBioScience) and 50 µg/mL mitomycin C (Sigma Aldrich) was added to the growth medium to inhibit the cell proliferation. Images were

taken every 2 hours for 16 hours at 4X magnification with IncuCyte ZOOM Live-Cell Analysis System (EssenBioScience). After background and cell debris subtraction, wound closure was determined with the IncuCyte ZOOM Software (EssenBioScience). At least two biological replicas with three technical replicas each were shown for every experiment.

Invasion Assay

$5x10^3$ E16.5 WT NSPC or mGIC cells were resuspended with 100 µL of the collagen gel mixture (4 mg/mL of Rat Tail Collagen Type I High Concentration (Corning) and 10% MEM (Gibco)) and plated in a 96-well plate. The mixture was spun for 10 minutes at 4°C, 1000 rpm. After 30 minutes incubation at 37°C, to allow the polymerisation of the collagen, growth medium was added on top of the gel in each well. 96 hours later, cells were then fixed with 4% PFA-PBS for 30 minutes at room temperature and stained with 1 ng/mL Hoechst (Sigma Aldrich) in 1X TNE buffer (Sigma Aldrich) for one hour at room temperature. Images were taken with the INCell 2200 (GE Healthcare) and analysis of the invading nuclei was performed with Developer Toolbox software (GE Healthcare) after background subtraction. Two biological replicas with at least two technical replicas each are shown for every experiment.

Neurosphere Formation Assay

$2.5x10^2$ mGIC were plated in each well of a 96-well plate and pictures were acquired using a Nikon Eclipse TE2000-S microscope after 96 hours in culture conditions. Neurosphere area and number were determined with ImageJ software. Two biological replicas with six technical replicas each are shown for every experiment.

Orthotopic transplantation of GIC into NODSCID mice and bioluminescence imaging (BLI)

All the *in vivo* procedures were carried out under Home Office approval (Animals Scientific Procedures Act 1986, PPL 70/7275 and P78B6C064). 6-12 week old NODSCID mice were anaesthetised with 6.4 µL per gram of body weight of the anaesthetic mixture (1mL of Narketan-10 (Vetoquinol), 0.5mL Rompun (Bayer) and 5.7 mL distilled water) by intraperitoneal injection. The scalp of each mouse was incised with a scalpel and the skull was exposed. 10 µl of sterile PBS containing $5x10^5$ mGIC were slowly injected with a 26 gauge Hamilton syringe needle into the right cerebral hemisphere with the following coordinates from the bregma suture: 2 mm posterior, 2 mm lateral, 4 mm deep, 10° angle.

The scalp was then sutured with 4-0 Coated Vicryl Suture (Ethicon) and the mice were allowed to recover on a heat-mat. Post-operative checks were performed twice a day for five days after surgery and every day thereafter. Mice were culled when symptomatic unless otherwise stated. Tumour formation and growth was assessed by BLI for mGIC xenografts. Mice were scanned every seven days from day 26 after transplantation, using IVIS Lumina III imaging system (PerkinElmer). Mice were intraperitoneally injected with 10 µL per gram of body weight of 15 mg/mL D-Luciferin D-Luciferin (Melford Laboratories) in DPBS (Gibco) and immediately anaesthetised with isoflurane (Abbott Laboratories). Images were acquired between 10 and 25 minutes after D-Luciferin injection, luminescence was recorded with a series of three minutes scans with large binning. Total flux (p/s) was measured with Living Image 4.3.1 software. To detect a reduction of an endpoint (Cohen's d [effect size] =2) at a statistical significance level (alpha level) of $p<0.001$ we estimated that 10 mice were needed per group, including mice added to compensate for anticipated losses (premature death, no graft growth, other losses [1].

Doxazosin level measurements in mice

Drug suspension: Each 50mg of doxazosin or elacridar (Insight Biotechnology) were dissolved in warmed DMSO, the resultant suspension was then vortexed with Kolliphor HS15 after heating to 50^{o}C then final injection mixture made up with warm PBS.

For experiments to determine doxazosin levels, experimental mice were subcutaneously injected with doxazosin at 50 or 100 mg/kg in 5% DMSO / 10% Kolliphor / PBS. Where concomitant doxazosin and elacridar was used, elacridar in 10% DMSO / 20% Kolliphor / PBS was administered by oral gavage four hours before doxazosin dose. 5% DMSO / 10% Kolliphor HS15 / PBS was used as a vehicle control for doxazosin and was used for a vehicle control for elacridar.

At stated time-points mice were culled with pentobarbital terminal anaesthesia and samples removed for doxazosin level assessment using published methods [13]. Blood was extracted by cardiac puncture and brains were removed. Blood was allowed to clot, centrifuged at 4,000 rpm for 10 min., and serum taken for analysis. Forebrain was dissected and weighed, then homogenised in PBS using a Qiagen TissueRuptor (9002757). After centrifugation, homogenate supernatant was then mixed 1:1 with chloroform, centrifuged at 15,000 rpm for 5 min. and the aqueous (top) portion was taken for drug measurement. Doxazosin levels

were then analysed using liquid chromatography – mass spectrometry at the QMUL Mass Spectrometry Laboratory, Mile End, UK.

In vivo treatment with doxazosin

Tumour naïve mice treated once daily for 21 days with 50mg/kg, and 12 days with 100mg/kg did not suffer any weight loss, or show any behavioural changes. For *in vivo* doxazosin treatment of tumours, 100mg/kg of doxazosin was given daily by subcutaneous injection and 100mg/kg elacridar was given by oral gavage every second or third day, 4 hours prior to doxazosin dose (for schematic see figure S8D). Mice were assigned to treatment groups keeping number of male and females in each group equal. Experimental animals (n=8 for each group) were treated with elacridar and vehicle control, or elacridar and doxazosin without blinding. Mice were culled after treatment and brains removed for histological assessment.

Immunohistochemistry quantification

Tumour area: Human vimentin immunohistochemistry slides were scanned on a slide scanner, then an analysis protocol was composed on Definiens software for automated area quantification. Proliferation: High powered fields were randomly captured in tumour areas (four per condition), and Ki67 positive cells were counted with ImageJ software. Investigators were blinded to the group allocation during the analysis.

Statistical analysis

Statistical analysis was performed using GraphPad software unless otherwise stated. Significance was determined with t-test, one-way ANOVA (with Sidak's test) or two-way ANOVA as appropriate, unless otherwise stated, and displayed as the mean ± standard error (SEM). $p < 0.05$ was considered significant. Significance was indicated with asterisks: *, $p < 0.05$; **, $p < 0.01$; ***, $p < 0.001$; ****, $p < 0.0001$. At least three technical and two independent biological replicates were used in each experiments. All variables were assumed to be normally distributed unless otherwise stated. Outliers were considered those data points furthest from the median value.

References

1 Acquati S, Greco A, Licastro D, Bhagat H, Ceric D, Rossini Z *et al*. Epigenetic regulation of survivin by bmi1 is cell type specific during corticogenesis and in gliomas. Stem cells (Dayton, Ohio) 2013; 31: 190-202.

2 Cuddapah S, Jothi R, Schones DE, Roh TY, Cui K, Zhao K. Global analysis of the insulator binding protein CTCF in chromatin barrier regions reveals demarcation of active and repressive domains. Genome Res 2009; 19: 24-32.

3 Dobin A, Davis CA, Schlesinger F, Drenkow J, Zaleski C, Jha S *et al*. STAR: ultrafast universal RNA-seq aligner. Bioinformatics (Oxford, England) 2013; 29: 15-21.

4 Durinck S, Spellman PT, Birney E, Huber W. Mapping identifiers for the integration of genomic datasets with the R/Bioconductor package biomaRt. Nat Protoc 2009; 4: 1184-1191.

5 Jacques TS, Swales A, Brzozowski MJ, Henriquez NV, Linehan JM, Mirzadeh Z *et al*. Combinations of genetic mutations in the adult neural stem cell compartment determine brain tumour phenotypes. The EMBO journal 2010; 29: 222-235.

6 Lawrence M, Huber W, Pages H, Aboyoun P, Carlson M, Gentleman R *et al*. Software for computing and annotating genomic ranges. PLoS Comput Biol 2013; 9: e1003118.

7 Marino S, Vooijs M, van Der Gulden H, Jonkers J, Berns A. Induction of medulloblastomas in p53-null mutant mice by somatic inactivation of Rb in the external granular layer cells of the cerebellum. Genes & development 2000; 14: 994-1004.

8 Ramirez F, Ryan DP, Gruning B, Bhardwaj V, Kilpert F, Richter AS *et al*. deepTools2: a next generation web server for deep-sequencing data analysis. Nucleic Acids Res 2016; 44: W160-165.

9 Robinson MD, McCarthy DJ, Smyth GK. edgeR: a Bioconductor package for differential expression analysis of digital gene expression data. Bioinformatics (Oxford, England) 2010; 26: 139-140.

10 Tarazona S, Furio-Tari P, Turra D, Pietro AD, Nueda MJ, Ferrer A *et al*. Data quality aware analysis of differential expression in RNA-seq with NOISeq R/Bioc package. Nucleic Acids Res 2015; 43: e140.

11 Yadirgi G, Leinster V, Acquati S, Bhagat H, Shakhova O, Marino S. Conditional activation of Bmi1 expression regulates self-renewal, apoptosis, and differentiation of neural stem/progenitor cells in vitro and in vivo. Stem cells (Dayton, Ohio) 2011; 29: 700-712.

12 Yu G, Wang LG, He QY. ChIPseeker: an R/Bioconductor package for ChIP peak annotation, comparison and visualization. Bioinformatics (Oxford, England) 2015; 31: 2382-2383.

13 Zhang P, de Gooijer MC, Buil LC, Beijnen JH, Li G, van Tellingen O. ABCB1 and ABCG2 restrict the brain penetration of a panel of novel EZH2-Inhibitors. Int J Cancer 2015; 137: 2007-2018.

14 Zhang Y, Liu T, Meyer CA, Eeckhoute J, Johnson DS, Bernstein BE *et al*. Model-based analysis of ChIP-Seq (MACS). Genome Biol 2008; 9: R137.